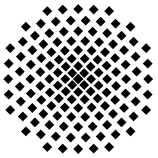

University of Stuttgart
Institute for Signal Processing and System Theory
Professor Dr.-Ing. B. Yang

Masterarbeit D1440

Improved Vital Sign Detection Using Millimeter Wave Radars

Verbesserte Vitalzeichenerkennung mit Millimeterwellenradar

Author: Yaseen El-Zawahry

Date of work begin: 01.02.2022
Date of submission: 14.07.2022

Supervisor: Prof. Dr.-Ing Bin Yang
M.Sc. Fady Aziz
M.Sc. Sherif Abdulatif

Keywords: Vital Signs, FMCW Radar

Acknowledgements

For all of the good songs that kept me motivated the whole time . . .

The Marshall Tucker Band - Can't You See
The Marshall Tucker Band - Take the Highway
The Marshall Tucker Band - 24 Hours at a Time
The Marshall Tucker Band - Am I the Kind of Man
The Marshall Tucker Band - Love is a Mystery
The Marshall Tucker Band - Walkin' the Streets Alone
Sergio Mendes - Pretty World
Sergio Mendes - Day Tripper
Sergio Mendes - Like a Lover
Sergio Mendes - Wave
Wilson Simonal - País Tropical
Wilson Simonal - Sá Marina
Catherine Warwick - Pollyanna
Katamari Damacy - Lonely Rolling Star
Emitt Rhodes - Somebody Made For Me
Emitt Rhodes - Promises I've Made
Jim Croce - Walkin' Back to Georgia
Chicago - Life Saver
Chicago - Color My World
Hubert Laws - Let Her Go
Herbie Mann - You Came a Long Way from St. Louis
El Dorado - Nelson Riddle
Billy Joel - Vienna
Billy Joel - Just the Way You Are
The Band - Ophelia
Randy Newman - Short People

Abstract

When the term *radar* is heard, it is natural for the typical reader to assume radar as applied for military and defense applications, such as detecting aircraft and missiles. The more informed reader could also be aware of radar applications in self-driving cars, commercial aviation, or even weather forecasting. However, few would be aware of the emerging applications of radar in the medical field. As quite recently there has been an increased focus in research about the usage of radar technology to measure vital signs. As the name suggests, vital signs are key indicators of an individual's health, and include, but are not limited to, breath and heart rate. Almost all devices currently in use to measure vital signs require to be in direct contact with the person whose vital signs are being measured, possibly adding a degree of discomfort, as well as reduced mobility. Such methods are called *contact-based* methods. The usage of radar, on the other hand, would represent a *contactless* method, which would have a great value in the medical field, since it would offer more comfort and freedom of mobility. However, matching the radar's degree of accuracy to that of traditionally used devices requires the development of robust and effective signal processing algorithms to convert the radar's raw signal into meaningful vital sign readings. This has been handled by previous work, and it has been demonstrated that accurate breath and heart rate estimations could be done with various radar technology. However, this was mostly limited to the measurement of the vital signs of one person in one orientation, mostly sitting down. In this work, we demonstrate how this may be extended for more than one person, in more than one physical orientation, and in more than one physical condition, all while still estimating the vital signs with satisfactory accuracy.

Contents

1 Introduction

Vital signs are measurements of the body's most basic functions, and include breath rate (BR), heart rate (HR), blood pressure (BP), and body temperature (BT). They are a reliable determinant of a person's health or the lack thereof. Medical conditions such as Obstructive Sleep Apnea Syndrome (OSAS) and Sudden Infant Death Syndrome (SIDS) are two major conditions causing high mortality in both infants and adults respectively [1]. According to [2] nearly a billion people are affected by OSAS around the world, and according to [3] SIDS is the leading cause of death of infants younger than 1 year old in the developed world. However, the monitoring of vital signs is essential for early detection of both OSAS [4] and SIDS [5], and also can be used for the prediction of certain pulmonary and cardiovascular diseases accounting for more than 31% of all deaths worldwide [6]. Such findings justify the necessity for continuous vital sign monitoring for infants and elderly patients. The measurement of body temperature is relatively simple, low cost, and does not often require to be continuously monitored. However, the detection and monitoring of the breath and heart rates and blood pressure usually require complex systems for continuous measurement. This thesis is focused on the measurement of the breath and heart rates, and so from this point forward the term *vital signs* will be used synonymously with the breath and heart rates.

1.1 Conventional Methods

This section reviews some of the major conventional methods used for detection human vital signs, highlighting the fundamental principles of the various methods as well as their shortcomings.

Electrocardiography

The basic principle of electrocardiography is the acquisition of the electrical activity of the heart that results from the action potential generated by heartbeats through measuring the potential difference between at least two points on the patient's body surface using contact electrodes [7]. The voltage signal obtained from an electrocardiography is referred to as an electrocardiogram (ECG). ECG systems are more commonly used to monitor heat rates, but also the breath rate can be estimated from ECG data [8].

Clinical ECG systems are considered the gold standard method of measuring the heart rate, but they are not without drawbacks. They are generally bulky and expensive. Also, traditionally, ECG systems increase their sensitivity by using conductive hydrogel between the contact electrodes and the patient's skin which has a toxic nature and can cause skin irritation for some patients [9].

Photoplethysmography

Photoplethysmography is an optical measurement method that is often used for heart rate monitoring purposes. Through a light source and a photo detector at the surface of the patient's skin, volumetric variations resulting for the patient's blood circulation are measured resulting in a so-called photoplethysmogram (PPG). This is possible because the intensity of the light reflected off the patient's skin varies with the patient's heart beat. The PPG signal is mainly used to estimate the heart rate, but still, the breath rate can be estimated from PPG data because of amplitude and frequency modulation of the received signal resulting from breathing.

Although photoplethysmography systems are considered a cost-effective solution, they most often produce signals that are affected by several factors including the measuring site, ambient temperature, and the posture of the subject [10] [11] [12].

Airflow Sensing

The concept of airflow sensing relies on measuring the characteristics of the inhaled an exhaled air such as its carbon dioxide (CO_2) concentration, temperature, and humidity, each of which vary between the exhalation and the inhalation phase. Capnography is used to estimate the patient's breath rate from CO_2 variations between the inhaled and exhaled air, commonly through an infrared sensor. Inhaled and exhaled air typically contain approximately 0.04% and 6% CO_2 respectively [13]. Similarly, the difference in temperature and/or humidity of inhaled and exhaled air can be utilized to measure the breath rate.

Airflow sensing is a simple technique, especially when measuring airflow temperature, since it's the simplest and most cost effective in general [1]. However, such breath rate detection systems require the patient to wear a face mask or a tube around the nostril, which is quite uncomfortable for long-term monitoring. Also, such airflow characteristics are sensitive to environmental variations such as presence of other gas components and changes in humidity and temperature of the environment [14].

Chest-wall Mechanical Displacement Sensing

The contraction and expansion of the diaphragm during normal human respiration result in the displacement of the chest that can expand up to 7.37 cm circumferentially [15]. Several types of sensors can be used to detect this chest-wall motion, which is also affected by the motion of the heart beat, and so such a measurement can be used to measure the heart rate. The most common method of measuring the chest-wall displacement is based on strain-sensing, which employs resistive sensors to record the instantaneous change in strain of a belt strapped around the chest.

Although chest-wall mechanical displacement sensing is able to deliver accurate readings for the breath rate, it still suffers from the discomfort and awkwardness associated with wearing such a belt around the chest for extended periods of time for long-term monitoring of the breath rate.

Blood Pressure Sensing

Sensing blood pressure can be used to measure the heart rate. This is because the rhythmic pulsation of the heart causes pressure of blood on the walls of blood vessels. An appropriately placed sensor (e.g. on the wrist) can be used to capture the instantaneous blood pressure resulting from the heartbeat [16]. Such a sensor can be based on palpatory and ultrasonic methods, among others. In the palpatory method, an inflatable cuff is placed around the upper arm of the subject, and a manometer connected to the cuff is used to measure the pressure. In the ultrasonic method is based on the Doppler effect where the ultrasonic frequency shift due to blood movement is proportional to the velocity of the blood flow in the vessel, this method also involves the use of a cuff [17] like the palpatory method.

Blood pressure sensing is able to measure the blood pressure in an automated manner and can deliver accurate results. However, inaccuracies can occur due to misalignment of the cuff [18]. Also, like the previously mentioned methods, this method is not practically desired for extended durations due to the discomfort that comes with wearing the cuff around the upper arm.

Sound-based Sensing

The heart produces sounds that can be detected by a microphone as it beats resulting from contraction and relaxation of the heart muscle, the rising and falling pressures of the cardiac cavities, the opening and closing of the valves, and the blood circulating and stopping. This detection of the heart rate based on cardiac sounds is called phonocardiography (PCG). Recording this cardiac acoustic phenomena may help cardiac events be visualized [19]. PCG is able to pick up abnormalities in cardiac sounds, often referred to as murmurs, which can be indicators of disease [20].

PCG curves demonstrate cardiac patterns comparable to the ECG acquisition system. However, PCG failed to keep up with standardization due to the emergence of other cardiac signal assessment methods [21], despite its wide applications in the early twentieth century. The system is also vulnerable to surrounding acoustic effects and sounds from respiration that are much stronger than the cardiac sounds.

1.2 Aim

Although all of the aforementioned methods possess a medium to high accuracy of measuring vital signs, they all suffer from a common drawback, being the fact that they are all *contact-based* methods, since they all require the use of contact senors. Such contact-based methods may introduce a degree of discomfort, as well as reduced mobility for the patient. This is made worse for long-term monitoring, and makes repeatable measurement less practical. They can also cause unnecessary further distress for the patient. A typical contact-based method is illustrated in Fig. 1.1.

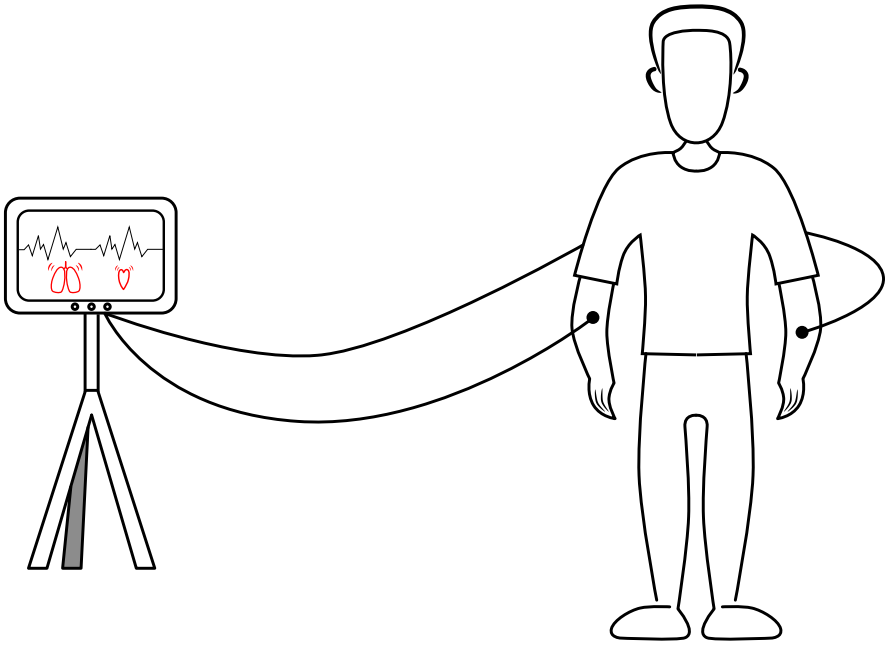

Figure 1.1: Illustration of contact-based methods.

For those reasons, many recent research has been focused towards the development of *contactless* cardio-respiratory monitoring systems that use radar technology. As the name suggests, contactless monitoring systems do not require any attachment or contact whatsoever between the measuring device and the patient. This forward step in vital sign measurement preserves the patient's comfort and freedom of mobility, and is also more suited for long-term monitoring and repeated measurement. This idea is illustrated in Fig. 1.2

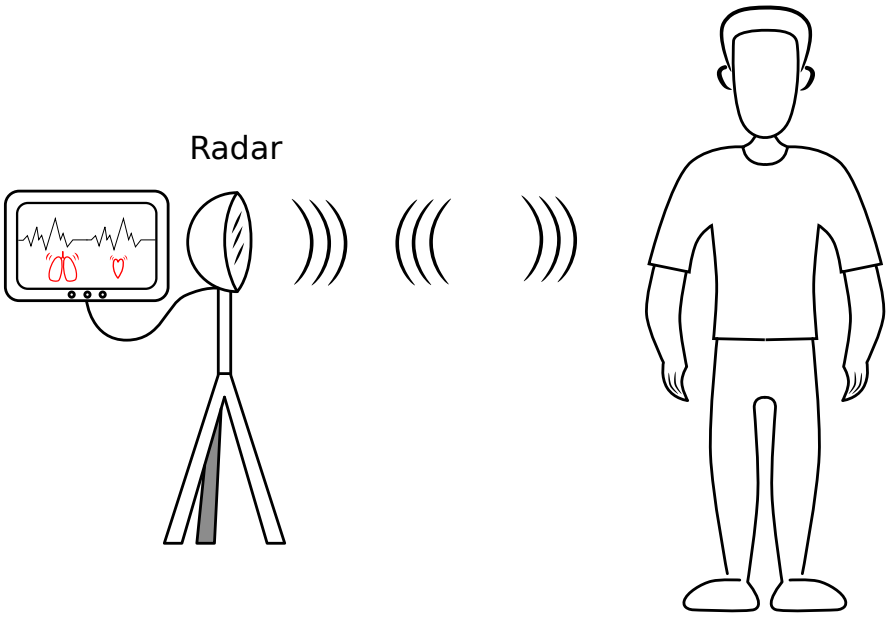

Figure 1.2: Illustration of contactless methods.

Contactless radar-based vital signs detection relies on the modulation effect of a radio signal sent by a transceiver towards the patient due to their chest-wall displacement, which is affected by the breath and heart motion, along with environmental and electronic noises. The typical transmitted power by the radar does not exceed 12 dBm for a two-meters distance application, which is less than the power emitted by the average smartphone [1], therefore such radars are safe. Depending on the characteristics of the transmitted signal, the radar can be of type continuous-wave (CW), ultra-wideband (UWB), stepped-frequency continuous-wave (SFCW), or frequency-modulated continuous-wave (FMCW). The type of radar used in this work is an FMCW radar.

Regardless of the type of radar used, a reliable signal processing algorithm is needed to convert the raw radar readings into accurate vital sign readings for both the breath and the heart rates. Such a reliable algorithm needs to give accurate readings regardless of the patient's physical orientation (e.g lying, sitting, and standing) and regardless of the patients' breath rate range (e.g. hypo-, normal, or hyper- ventilation) and similarly for the patients' heart rate range. Also, the ability of the algorithm to measure the vital signs of more than one target at the same time is a plus, as this could allow for a more cost-effective solution. A use for this could be measuring the vital signs of several babies in a hospital's nursery room using one radar.

This work focuses on extending previously existing vital sign signal processing algorithms to allow for measuring the breath and heart rates for more than one person, and more than one orientation, all while preserving the accuracy for a wide range of breath and heart rates, using an FMCW radar. It is worth mentioning that such radar-based vital sign detection is not only limited for applications in the medical field. Such a system could be used for driver alertness monitoring to detect driver drowsiness and sleepiness to avoid auto accidents; for detecting persons who are either buried in emergency accident situations; in law-enforcement for detecting persons in hiding to resolve a security situation.

1.3 Related Work

CW radars are the most common type of radar due to their simplicity [1]. They have been proven able to detect vital signs successfully in several works of research such as [22] and [23]. CW radars, however, lack a necessary property, being the ability to detect multiple targets simultaneously, which is a necessary property to detect the vital signs of more than one patient simultaneously. For this reason, a CW radar was not chosen for this project.

In [24] a simple UWB radar employing body movement cancellation was designed and was able to detect the breath and heart rate, but even though the results appear to be good, the system is not suitable for real-world applications. In [25] a new algorithm is proposed which is based on multiple higher order cumulant, which gives a higher signal-to-noise ratio. The ability of the UWB radar pulse to penetrate walls and other concrete objects gives UWB radars an advantage for search and rescue or security operations [26]. However the problem with UWB radars is their high power density which needs to be limited due regulations, which limits them to short distance vital sign detection applications [1].

SFCW radars have been studied for biomedical applications, for example in [27] experiments were conducted using an SFCW radar to obtain the breath and heart rates of three individuals at the same time. In [28] an SFCW radar showed capability of non-line of sight detection of human respiratory signals, showing a potential of SFCW radars being used in the application of search and rescue during natural disasters like earthquakes. Although it would have been a good candidate for this work, SFCW radar hardware was not accessible, and so could not be used.

FMCW radars are capable of providing range and velocity information, and therefore are able to track multiple targets, and so are able to detect the vital signs of more than one patient. The authors of [29] used an auto-regression algorithm to extract the breath and heart rates. The work of [30] uses multiple antennas to detect and locate the vital signs of two subjects. The work of the master thesis [31] modifies on the algorithm of [30] by adding Kalman filtering to improve breath rate readings for standing subjects. The work we present in this thesis is based largely on the work of [30] and [31].

1.4 Thesis Outline

This thesis is divided into five chapters in total, including the introduction, and the remainder of the document is structured as follows:

Chapter 2 This chapter presents the reader to the background of the FMCW radar's theory of operation that is essential to understand how raw data is collected using such a radar.

Chapter 3 This chapter slowly builds our signal processing chain step by step, explaining the importance of each step, until the whole chain is presented.

Chapter 4 This chapter discusses the experiment's setup along with the results of experimentation. It also demonstrates the GUI application created for real-time vital sign estimation.

Chapter 5 This chapter presents a summary of the work discussed and demonstrated in this thesis along with the conclusion of the work and recommendations for future.

2 FMCW Radar Theory

Radars work by transmitting an electromagnetic signal which, in turn, gets reflected back by any objects in the path of the signal. By capturing and processing those reflected signals, the radar system can determine properties of those objects, this is illustrated in Fig. 2.1. FMCW radars are able to estimate the range, velocity, and incidence angle of those objects. FMCW radars also posses a millimeter level precision in object range detection that makes such a radar an ideal piece of technology for sensing a subject's vital signs, as will be shown later. In this chapter we present the basics of how an FMCW radar works; from transmitting an electromagnetic signal up until it delivers a raw reading.

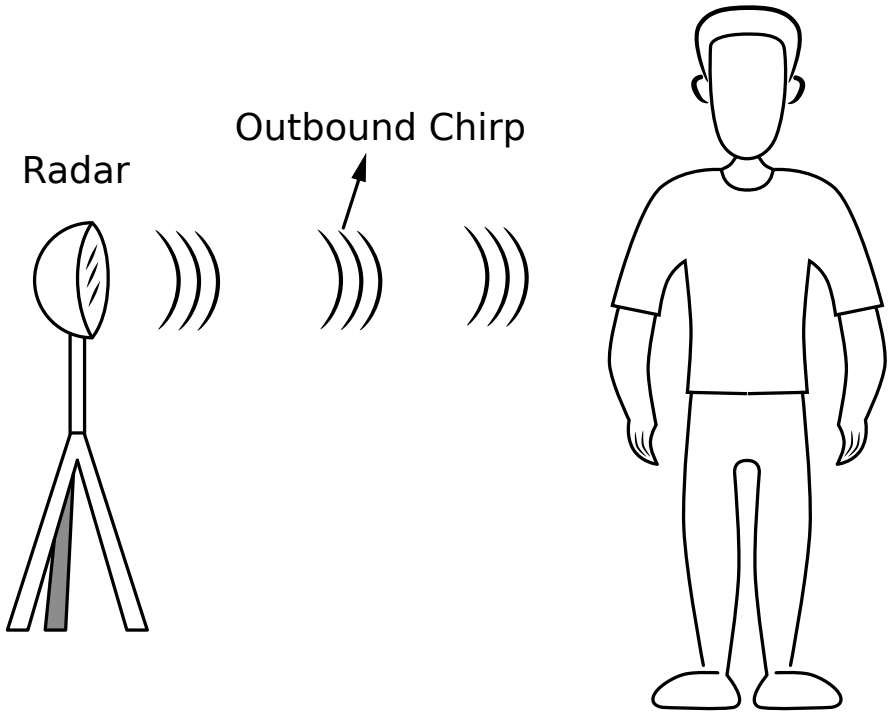

Figure 2.1: Illustration of a generic radar.

Fourier Transform

Before discussing the FMCW radar's theory of operation, it is essential to first explain the Fourier transform (FT), since it is an important mathematical step taken several times during obtaining the raw radar reading, and the breath and heart rates. The FT is a mathematical transform which decomposes a function depending either on space or time into a function that depends on spatial frequency or temporal frequency respectively [32]. The FT of a function will output a complex valued function which represents the complex sinusoids that make up the original function.

The FT has a continuous and a discrete variant. The continuous variant is concerned with continuous input functions of the form $x(t)$ where $x \in \mathbb{R}$, whereas the discrete variant is concerned with discrete input functions of the form $x[n]$ where $n \in \mathbb{Z}$. In this thesis we are concerned with the discrete variant, the Discrete Fourier Transform (DFT), which mathematically can be described for a finite sequence of length N as

$$X[k] = \sum_{n=0}^{N-1} x[n] e^{-j2\pi kn/N} \tag{2.1}$$

for all $0 \leq k < N$ and is equal to 0 otherwise. Note that the DFT of a sequence $x[n]$ of length N is the sequence $X[k]$ of also length N. There exist a class efficient algorithms to compute (2.1), this class of algorithms is called the Fast Fourier Transform (FFT). Recall that the output of the FT is a complex number which can generally be represented in the phasor form as

$$X[k] = A(k)e^{j\theta(k)} \tag{2.2}$$

2.1 The Chirp

At the heart of the FMCW radar is a signal called a chirp. Similar to how a bird sings out a chirp, a sound wave for the sake of communication in this case, the FMCW radar radiates its version of the chirp; an electromagnetic wave which gets reflected off objects, whose detected reflection is used to estimate those objects' ranges, velocities, and angles of incidence.

The FMCW radar's chirp is visualized in an amplitude vs. time plot in Fig. 2.2, were it can be seen that the chirp is a sinusoidal signal whose frequency increases with time. The properties of this frequency-increasing sinusoidal signal are made clearer in Fig. 2.3, from it, it can be seen that the frequency of the chirp increases linearly with time.

The chirp's defining mathematical properties are also shown in Fig. 2.3. The start frequency f_c is the frequency at which the transmitted wave starts. The frequency of the wave increases linearly with time with a slope S for a time duration of T_c time units. The difference between the ending frequency and the starting frequency is the bandwidth B.

The FMCW radar will transmit a chirp signal, which will subsequently get reflected off surrounding objects in the radar's field of view. The reflection off an object is received by the radar a fraction of a second later, which is merely a delayed version of the transmitted signal. This is shown in a frequency vs. time plot in Fig. 2.4. The subsequent signal processing of this reflected signal, as well as others reflected off other objects, enables the estimation of a target's range information.

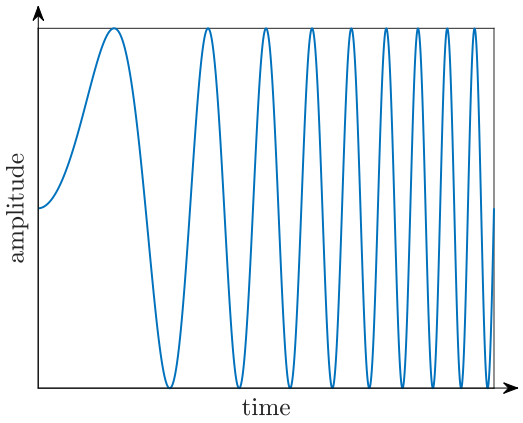

Figure 2.2: A single chirp visualized in an amplitude vs. time plot.

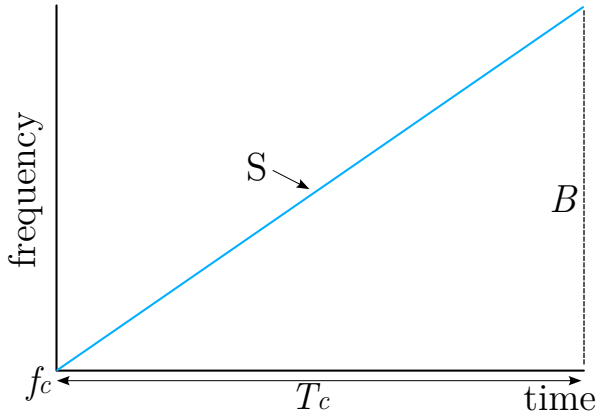

Figure 2.3: A single chirp visualized in a frequency vs. time plot.

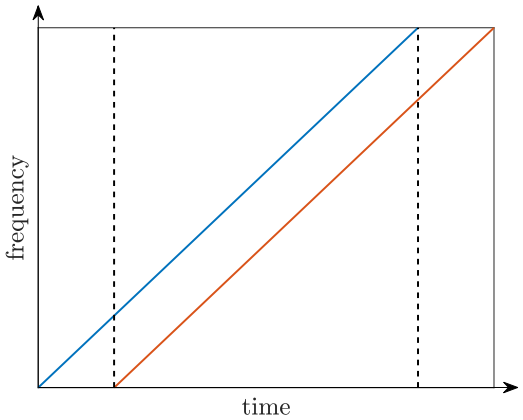

Figure 2.4: The transmitted and reflected chirps plotted in blue and red respectively.

During normal operation of the FMCW radar, multiple chirps will be transmitted by the radar one after the other in a way similar to that shown in Fig. 2.5, with each chirp's subsequent reflections off objects getting picked up by the radar and subsequently processed.

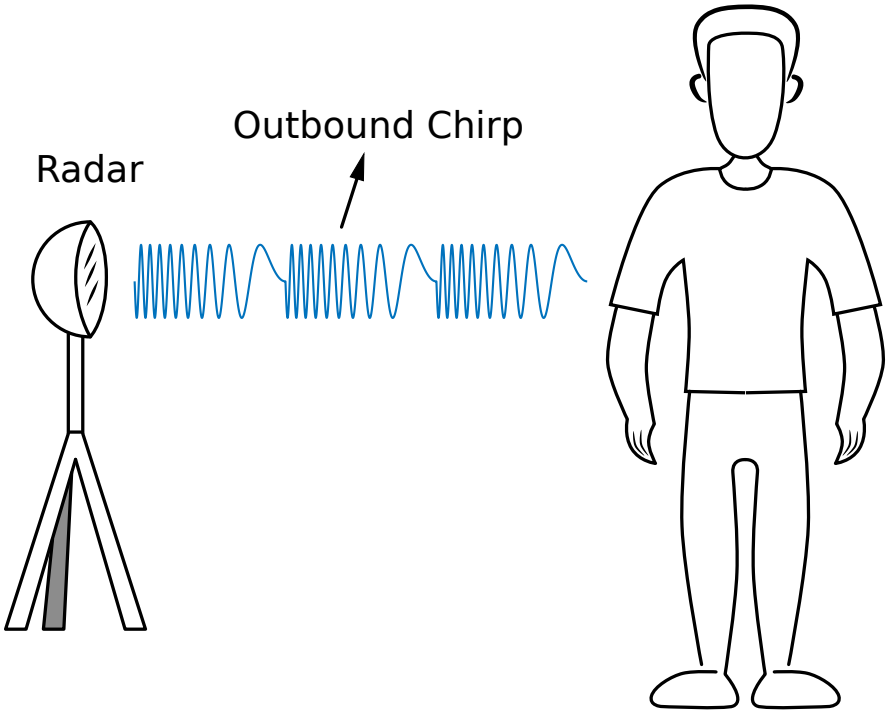

Figure 2.5: Many chirps will get transmitted by the radar one after the other.

2.2 Radar Components

Now that the shape and structure of the chirp have been presented, we now proceed to introduce the components of the FMCW radar. The five main components are: the chirp synthesizer, the transmitter (TX) antenna, the receiver (RX) antenna, the mixer, and the Analog-to-Digital Converter (ADC). The block diagram of this structure is shown in Fig. 2.6.

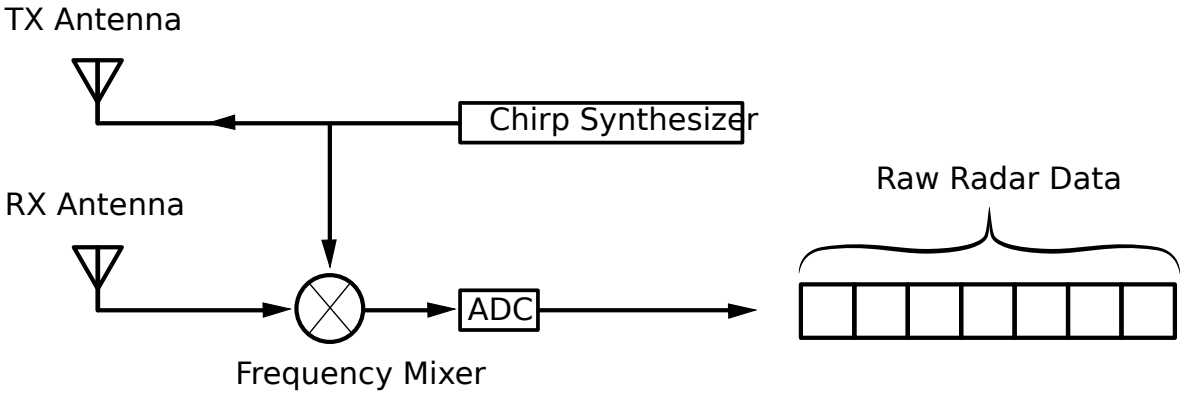

Figure 2.6: Diagram of a radar with one RX antenna.

It all begins with the chirps synthesizer which generates the chirp signal as an electrical signal. This electrical signal is then transmitted as an electromagnetic signal by the TX antenna. The chirp radiates across the radar's field of view, and is reflected by objects back towards the radar, where it is picked up by the RX antenna, and is converted to an electrical signal again.

The currently being transmitted and received electric signals are inputs to a frequency mixer, which shall be explained in the next section. The output of this frequency mixer is sampled over the duration of the chirp by the ADC, which results in a 1D matrix of values every chirp, which is the raw radar data.

Most of the time FMCW radars will have more than one RX antenna, which allows the estimation of objects' angles of incidence. Each RX will have a corresponding frequency mixer and an ADC unit, and so the resulting raw radar data will be a 2D matrix of values, this is shown in Fig. 2.7.

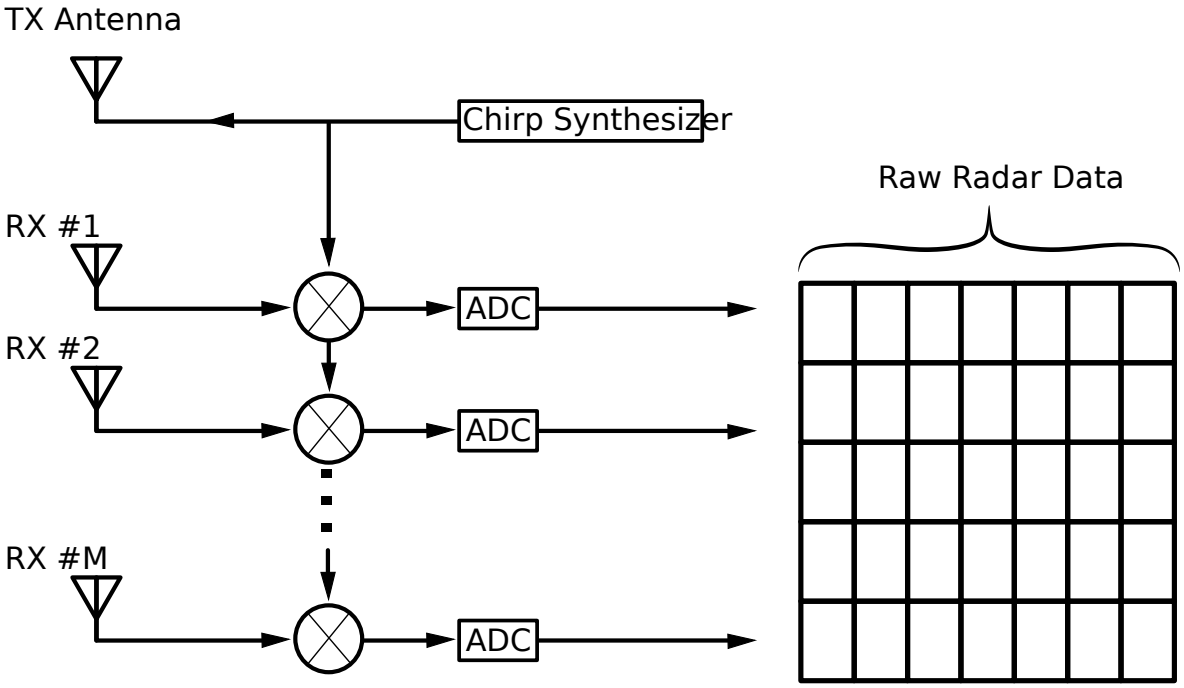

Figure 2.7: Diagram of a radar with multiple RX antennas.

2.3 The Frequency Mixer

As mentioned in the previous section, the inputs to the frequency mixer are the currently being transmitted and received electric signals, corresponding to the outbound and the inbound chirps respectively. The mixer works as follows: if the transmitted signal is represented as

$$x_{TX} = sin(2\pi f_{TX} t + \phi_{TX}) \tag{2.3}$$

and the received signal (from one object) is represented as

$$x_{RX} = sin(2\pi f_{RX} t + \phi_{RX}) \tag{2.4}$$

Then the output of the mixer, which is called the Intermediate Frequency (IF) signal, will be

$$x_{IF} = sin[2\pi(f_{TX} - f_{RX})t + (\phi_{TX} - \phi_{RX})] \tag{2.5}$$

which is equivalent to

$$x_{IF} = sin[2\pi f_{IF} t + \phi_{IF}] \tag{2.6}$$

The mixer output corresponding to a chirp received from one object will be a constant frequency value, as seen in Fig. 2.8, since the value of f_{IF} is $(f_{TX} - f_{RX})$ which is the difference between two parallel lines, which in turn is a constant value.

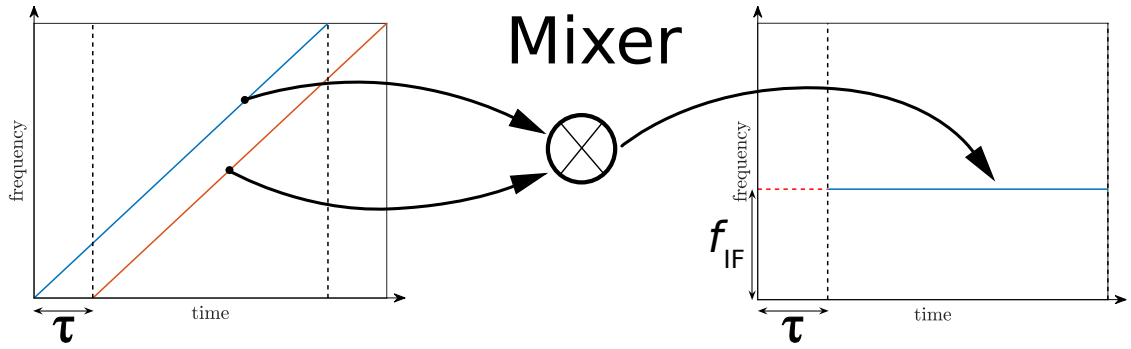

Figure 2.8: Output of the mixer given an outbound and inbound chirp.

The value of this constant-valued frequency tone f_{IF} is a function of the round trip time between the radar and the object τ, and the slope S of the chirp. So, if the distance of the object from the radar is d (also called range) and the speed of light is c, then $\tau = 2d/c$ and so the IF can be calculated from

$$f_{IF} = S\tau = S\frac{2d}{c} \tag{2.7}$$

where it can be seen that the value of f_{IF} is proportional to the range of the object d. The value of τ is typically a small fraction of T_c and is approximately 5%.

2.4 Range Estimation

The estimation of the range of an object given a corresponding IF signal is done by applying the FFT on the ADC sampled IF signal, which is the 1D radar raw data (in the case of one RX antenna). Since the IF is consisted of one frequency, therefore the amplitude vs. frequency plot of the FFT's output will have an amplitude peak at frequency with value equal to f_{IF} as shown in Fig. 2.9.

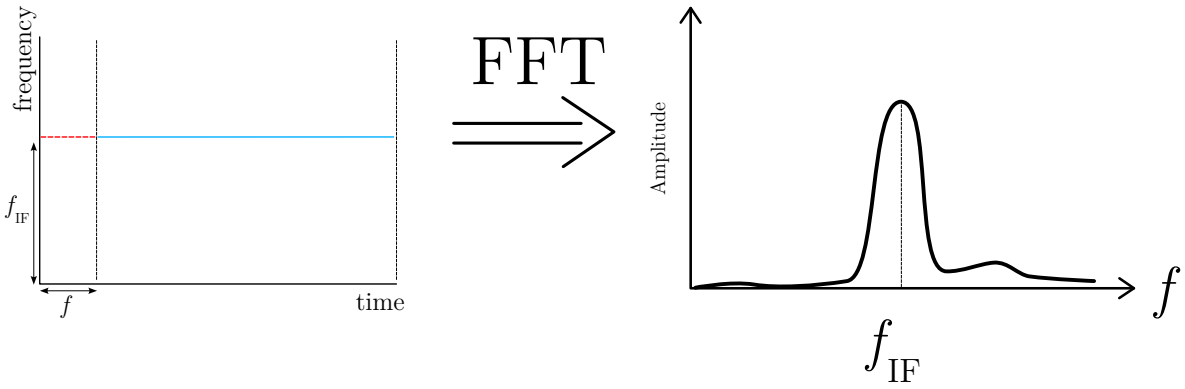

Figure 2.9: Applying the FFT on a sampled IF signal corresponding to one object.

Since the range d and the IF signal frequency f_{IF} are linearly related as shown in 2.7, then the FFT's output from Fig. 2.9 is equivalent to the amplitude vs. distance plot shown in Fig. 2.10. This plot is called a range profile. A distance in this range profile which corresponds to an amplitude peak also corresponds to the range of an object. In the presence of more than one object, the range profile will be similar to what is shown in Fig. 2.11, where we have three peaks corresponding to three different objects, for the sake of giving an example.

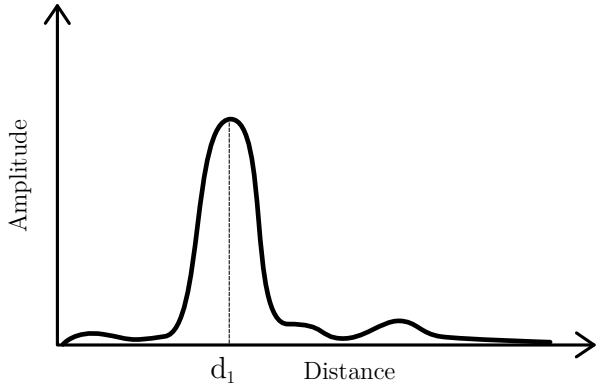

Figure 2.10: Range profile corresponding to one object.

Range Resolution

As two objects more closer together, their corresponding peaks in the range profile will also move closer together. Two objects who are somewhat close may have a range profile similar to Fig. 2.12, where the peaks are close, but still they are still distinguishable from one another. However, if those objects are too close together, this will cause their corresponding peaks in the range profile to combine into one peak, diminishing the ability to detect two different objects from the range profile alone. This will result in a range profile similar to Fig. 2.13.

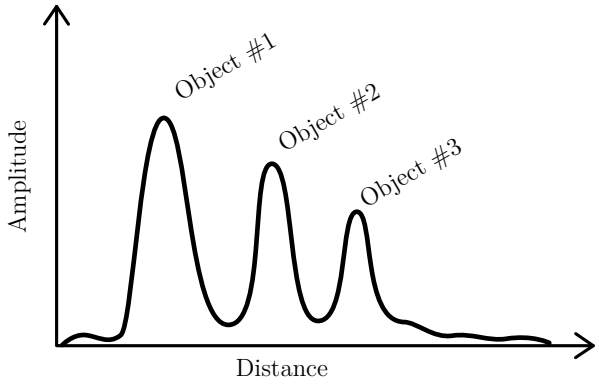

Figure 2.11: Range profile corresponding to three objects.

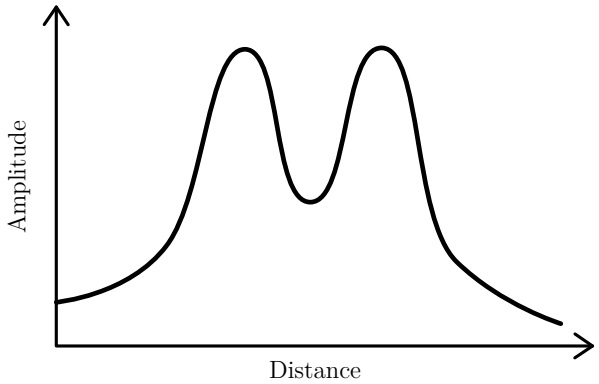

Figure 2.12: Peaks of two somewhat close objects.

This brings us to the concept of *range resolution*. It is the minimal distance by which two different objects should be separated in order for them to be manifested as two different peaks in the range profile. To mathematically find the range resolution of the radar, we first acknowledge that the result of the FFT of a signal observed for T time units can, logically, only distinguish between two frequency components separated by a minimum of Δf which must satisfy

$$\Delta f > \frac{1}{T} \tag{2.8}$$

and so to distinguish between two IF frequencies corresponding to two different objects we need to have

$$\Delta f_{IF} > \frac{1}{T_c} \tag{2.9}$$

We substituted T for T_c in 2.9 since the IF signal is observed during the chirp duration. We can deduce from 2.7 that

$$\Delta f_{IF} = S\frac{2\Delta d}{c} \tag{2.10}$$

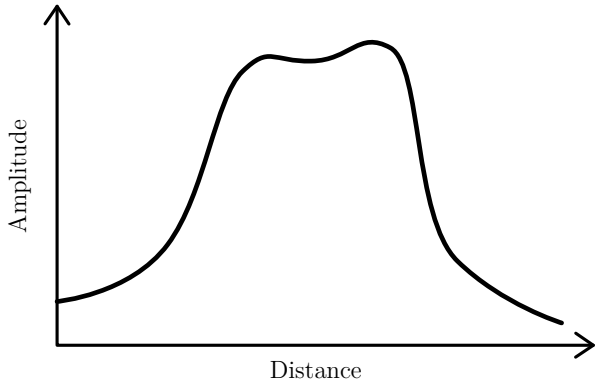

Figure 2.13: Peaks of two too-close objects.

and so from 2.9, 2.10, and the fact that $B = S T_c$ we have

$$\Delta d = d_{res} = \frac{c}{2B} \tag{2.11}$$

From 2.11 we can see that the range resolution d_{res} is dependant only on the chirp's bandwidth B, which is in turn dependent only the chirp duration T_c and slope S. Meaning, that in order to improve the range resolution, and so allow objects to be closer together and still be distinguishable from one another, we can either increase the chirp duration T_c, the chirp slope S, or both.

2.5 Signal Phase

Up until this point we have only studied the amplitude component of the FFT's output which is given by $A(k)$ from 2.2, which has enabled us to produce a range profile from the radar's raw IF signal. However, studying the phase component $\theta(k)$ allows us to go further in terms of signal processing, since knowledge of the phase allows us to additionally estimate objects' velocities, angles of arrivals, and also allows for measuring very small displacements in range. The kth element of the FFT's output of the IF signal of the lth chirp can be mathematically described as:

$$X[k, l] = A(k, l)e^{j\theta(k,l)} \tag{2.12}$$

Here k shall be referred to as the range bin index, since it refers to an IF frequency index which in turn corresponds to a range value by virtue of 2.7. The index l shall be referred to as the chirp index. The phase difference of an object at a given range bin index between two successive chirps shall therefore be defined as

$$\Delta\phi = \theta(k, l + 1) - \theta(k, l) \tag{2.13}$$

This phase change $\Delta\phi$ for a given object at a certain range bin index is given without proof by

$$\Delta\phi = \frac{4\pi\Delta d}{\lambda} \tag{2.14}$$

where Δd is the change in range and and λ is the carrier frequency wavelength.

Note that although 2.14 may be similar to 2.11 in terms of both referring to Δd, each refers of a different meaning of Δd. In 2.11, the value of Δd refers to the range resolution; the minimum distance between **two** objects such that they manifest as two different peaks in the range profile. In 2.14, on the other hand, Δd refers to the change in range of **one** object between two successive chirps.

Note also, that mathematically, it is also possible to calculate Δd by observing changes in f_{IF} and using 2.10. However this would mean observing very small Δf which would require a much larger observation time, and so a much larger value of the chirp duration T_c. However, monitoring the phase of an object at a certain range bin index k allows us to monitor very small deviations in range Δd. This is because the value of λ is typically very small (in the order of 10^{-9}), and so a small change in range Δd would correspond to a large change in phase $\Delta\phi$. Meaning that the phase of a range bin value corresponding to **one** object is very sensitive to changes in range of that same object.

So, it should be noted that 2.7 should be used in estimating the range of an object, ignoring small variations in range causes by small motion, and that 2.14 should be used to monitor small variations in range caused by small motion, like the motion of the chest wall due to breathing or the beating of the heart, as will be shown later in this thesis.

2.6 Angle Estimation

Alongside the range information of an object, an FMCW radar is able to measure objects' velocities and angles of incidence. Velocity estimation is irrelevant for this thesis, and so will be skipped. This section will introduce the estimation of objects' angles of incidence. Note that the term *angle* will be used synonymously with *angle of incidence* throughout this thesis.

For range estimation, the use of only one RX antenna was needed. Angle estimation, however, requires at least two RX antennas. A radar with more than one TX antenna and more than one RX antenna is classified as a Multiple Input Multiple Output (MIMO) radar (note that for angle estimation only one TX will be enough). Assume a radar with one TX antenna and two RX antennas as shown in Fig. 2.14. The range of the object as seen by RX_1 will be d, and since RX_2 is a bit further from the object, its range will be $d + \Delta d$.

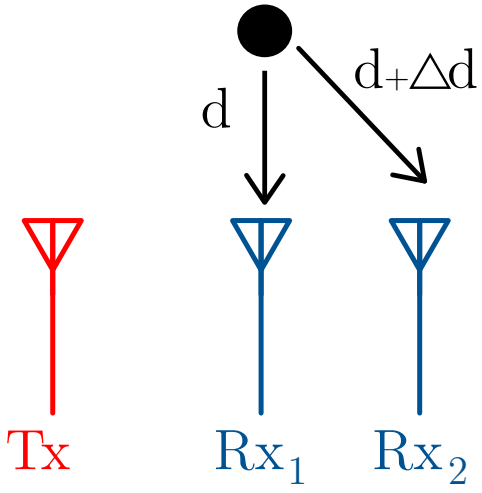

Figure 2.14: A radar with two RX antennas.

Now, if the object being detected is sufficiently far away from the radar and/or sufficiently bigger than the inter-antenna spacing a, then the electromagnetic rays to and from the radar could be assumed parallel, and so the distances can be as shown in Fig. 2.15.

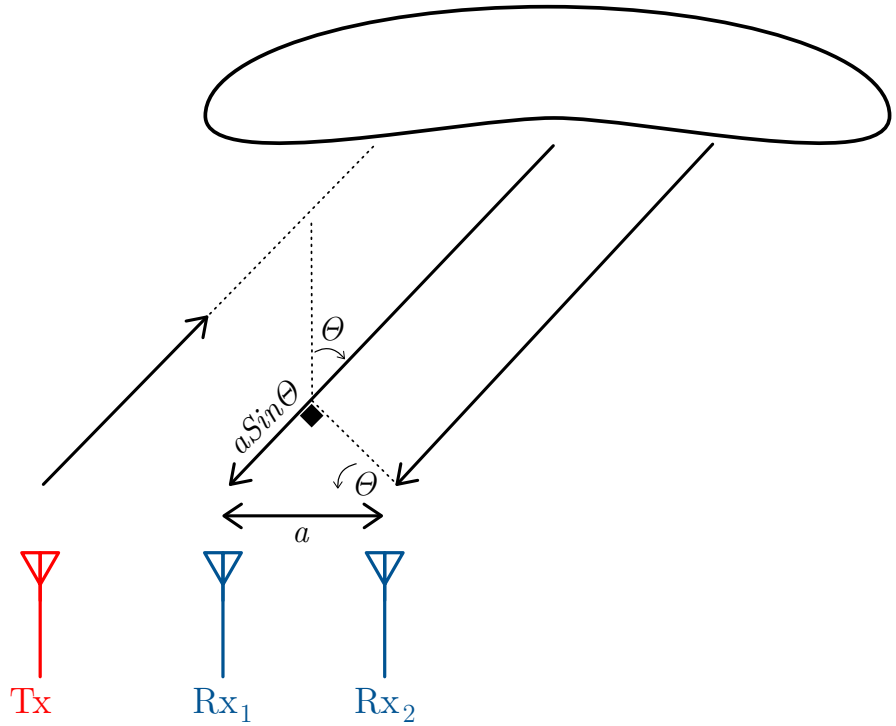

Figure 2.15: Outbound and inbound rays for a sufficiently far object.

Here it is seen that the difference in range Δd seen by RX_1 and RX_2 is $asin(\theta)$. We can extend 2.12 for the case of multiple RX antennas by adding an RX antenna index m, and so we have

$$X[k, l, m] = A(k, l, m)e^{j\theta(k,l,m)} \tag{2.15}$$

and so for an object at the kth range bin index, for the lth chirp, the difference in phase $\Delta\phi$ of two RX antennas with antenna indexes m_1 and m_2 can be defined as

$$\Delta\phi = \theta(k, l, m_1) - \theta(k, l, m_2) \tag{2.16}$$

This phase difference between the two antennas for the same chirp and object is given without proof by

$$\Delta\phi = \frac{2\pi\Delta d}{\lambda} = \frac{2\pi a sin(\theta)}{\lambda} \tag{2.17}$$

Where Δd is the object's range difference between the two RX antennas as depicted in Fig. 2.15 and λ is the carrier frequency wavelength. Note the similarity of 2.17 and 2.14. In 2.14 the phase difference $\Delta\phi$ refers to the phase difference between two successive **chirps**. However, in 2.17 the phase difference is between two **antennas** (which are not necessarily adjacent). We can rearrange 2.17 to obtain:

$$\theta = sin^{-1}\left(\frac{\lambda\Delta\phi}{2\pi a}\right) \tag{2.18}$$

The general case of multiple equally spaced RX antennas is visualized in Fig. 2.16. If RX_1 has phase ϕ_1, then RX_2 has phase $\phi_1 + \Delta\phi$, RX_3 has phase $\phi_1 + 2\Delta\phi$, and so on until RX_M has phase $\phi_1 + (M-1)\Delta\phi$. The constant phase difference between adjacent RX antennas is contingent on having a constant inter-antenna spacing a.

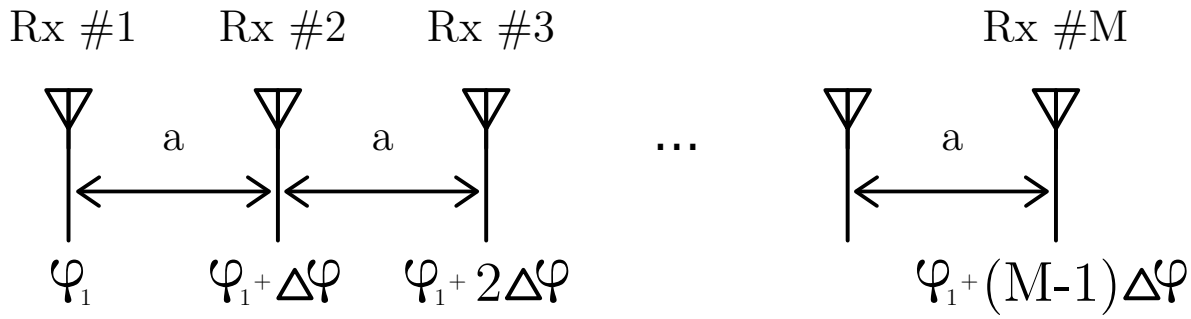

Figure 2.16: Phase difference between multiple RX antennas.

So if we hold the range bin index and the chirp index constant, and allow the phase from 2.15 to vary along the RX antenna index, we can give the phase as:

$$\theta(k, l, m) = \phi_1 + (m - 1)\Delta\phi = \theta(m) \tag{2.19}$$

since we are holding k and l constant. We can also similarly state that

$$A(k, l, m) = A(m) \tag{2.20}$$

We can assume that $A(m)$ stays almost constant across all values of m, since the very small variations of ranges of the object relative to the different RX antennas correspond to small variations of range profiles given by each RX antenna for one chirp, which is $A(m)$. This is shown in Fig. 2.17. So we can state that

$$A(m) \approx A \tag{2.21}$$

Substituting 2.19 and 2.21 into 2.15 gives:

$$X[k, l, m] \approx Ae^{j\theta(m)} = Ae^{j(\phi_1 + (m-1)\Delta\phi)} \tag{2.22}$$

Rearranging 2.22 according to Euler's formula gives us:

$$X[k, l, m] \approx A[cos((\Delta\phi)m + (\phi_1 - \Delta\phi))) + jsin((\Delta\phi)m + (\phi_1 - \Delta\phi))] = X[m] \tag{2.23}$$

So from 2.23 it is clear that we have sinusoidal variation of $X[k, l, m]$ along the m dimension (RX antenna dimension) with frequency component equal to $\Delta\phi$. This is why when a second FFT is taken along the m dimension (first time was across the t dimension), while holding k and l constant, and plot the amplitude of the result, we get a plot similar to Fig. 2.18, where we have an amplitude peak at the value of $\Delta\phi$.

Substituting this value of $\Delta\phi$ into 2.18 will then give us the corresponding angle of incidence for that object. Also, similar to how the IF frequency could be converted to the range d using 2.7 and so convert Fig. 2.9 into Fig. 2.10, we could do the same using 2.18 to convert Fig. 2.18 into Fig. 2.19. Such a plot shall be referred to as an angular profile.

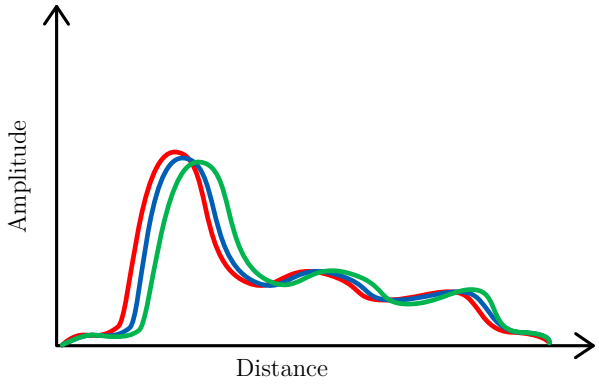

Figure 2.17: The range profiles from different RX antennas are almost the same.

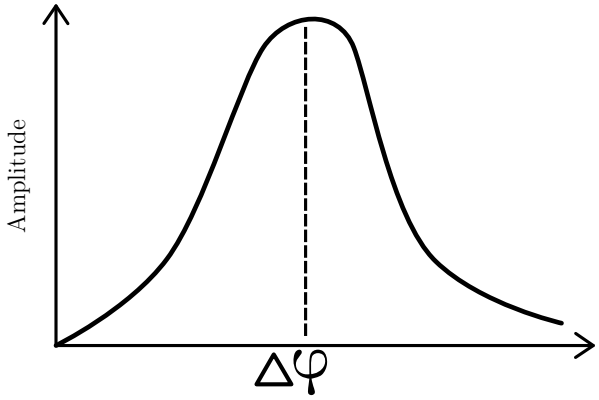

Figure 2.18: An amplitude peak is found at $\Delta\phi$.

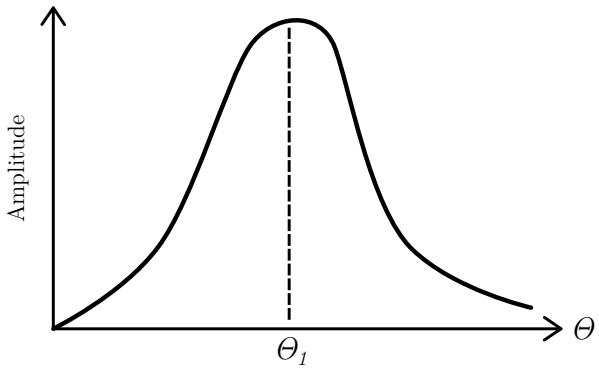

Figure 2.19: Angular profile corresponding to one object.

Angle Resolution

Similar to how we have range resolution, which is the minimum range separation between two objects such that they manifest as two different peaks in the range profile, we have angular resolution, which is the minimum angular separation between two objects needed such that they manifest as two different peaks in the angular profile. For simplicity, say that $\omega = \Delta\phi$, and so for M RX antennas we need to satisfy

$$\Delta\omega > \frac{2\pi}{M} \tag{2.24}$$

since it would not be possible to get a $\Delta\omega$ finer than $2\pi/M$, because we only have M antennas. Equivalently we could say

$$\Delta\phi(\theta + \Delta\theta) - \Delta\phi(\theta) > \frac{2\pi}{M} \tag{2.25}$$

which after substitution into 2.17 gives

$$\frac{2\pi a sin(\theta + \Delta\theta)}{\lambda} - \frac{2\pi a sin(\theta)}{\lambda} > \frac{2\pi}{M} \tag{2.26}$$

rearranging gives

$$\frac{2\pi a}{\lambda}[sin(\theta + \Delta\theta) - sin(\theta)] > \frac{2\pi}{M} \tag{2.27}$$

and then combined with the approximation

$$sin(\theta + \Delta\theta) - sin(\theta) \approx cos(\theta)\Delta\theta \tag{2.28}$$

gives

$$\frac{2\pi a cos(\theta)\Delta\theta}{\lambda} > \frac{2\pi}{M} \tag{2.29}$$

which can be simplified to give

$$\Delta\theta = \theta_{res} = \frac{\lambda}{Macos(\theta)} \tag{2.30}$$

We can infer a couple of things from 2.30. Firstly, the angular resolution is not constant, but actually a function of θ, and is highest at $\theta = 0$, directly in front of the radar, and reduces with angular deviation to each side. Meaning, that directly in front of the radar, two objects can be rather close and still get detected as two different objects, however, to the sides of the radar, those same two objects need to spatially separate more in order to ensure they still get detected as two different objects and not one. Secondly, what can be inferred from 2.30 is that the angular resolution can be improved by either adding more RX antennas (increasing M) or increasing the inter-antenna separation (increasing a), or both.

2.7 Range-Angle Heat Map

It was shown in the previous section that for obtaining an angle profile we fix the range bin index k and the chirp index l and then take a second FFT along the RX antenna index m, then the amplitude vs. angle plot can be obtained by plotting the amplitude of the output, and transforming the x-axis according to 2.18.

Similarly, we can create a two-dimensional heat map across the range and angle dimensions where "hot" areas indicate a presence of an object. This is done per chirp as follows: First, the radar will output a 2D matrix, the first dimension represents the RX antenna index m, and the second dimension represents the sample index n, as shown in Fig. 2.20.

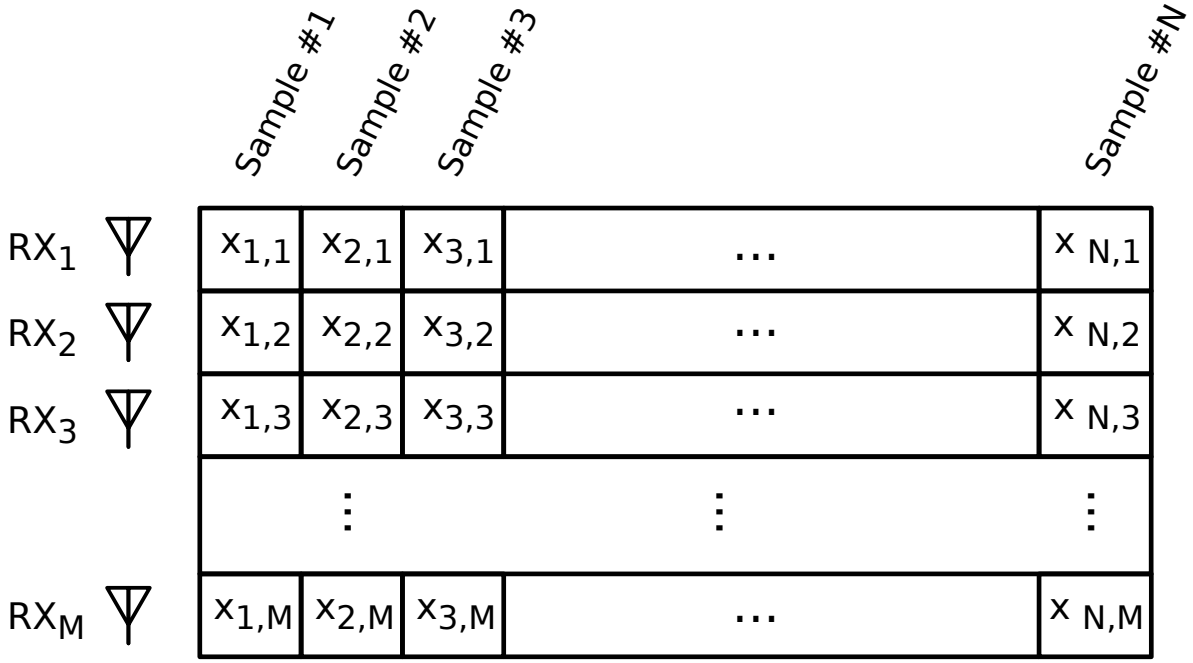

Figure 2.20: Raw data of radar with multiple RX antennas.

Afterwards, an FFT is applied across this 2D matrix along the sample dimension n, as shown in Fig. 2.21. Which results in another 2D matrix with values of the form $X[k, m]$.

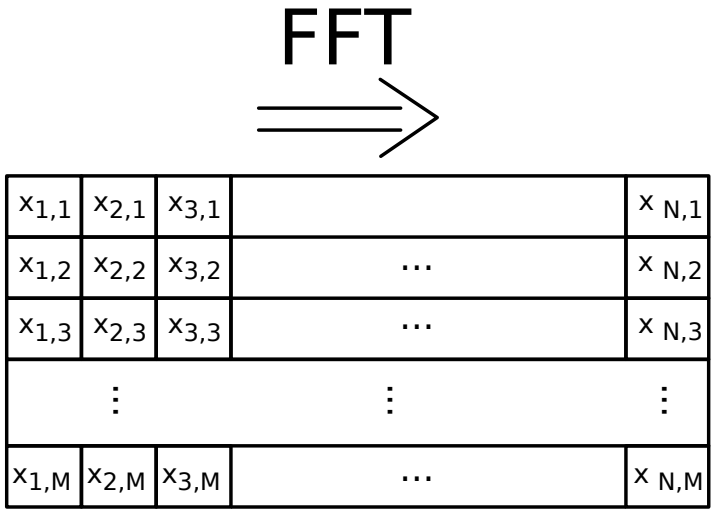

Figure 2.21: Applying the FFT across the n dimension.

Next, another FFT is applied but this time across the RX antenna dimension m, as shown in Fig. 2.22. Which results in another 2D matrix with values of the form $Y[k, m]$.

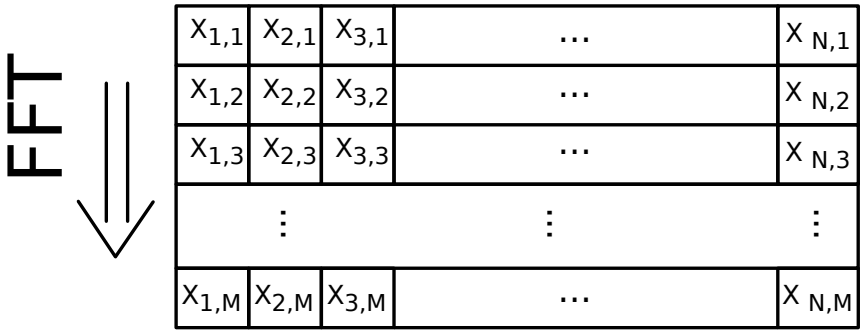

Figure 2.22: Applying the FFT across the m dimension.

The values of $Y[k, m]$, called range-angle bin values, are generally complex numbers. To convert to decibels, we apply the function $20log_{10}(|Y[k, m]|)$ to all the values in the matrix as seen in Fig. 2.23.

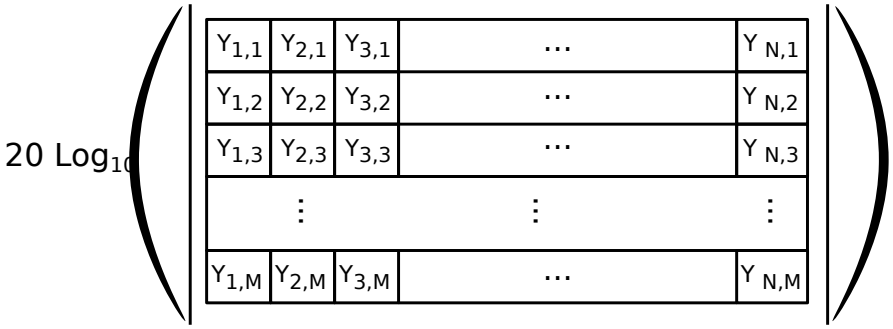

Figure 2.23: Converting to decibels.

This matrix of decibel values could be then plotted as a heat map. In an example where two subjects are positioned in front of the radar, one sitting and one standing, with a chair between them, we get a plot similar to that shown in Fig. 2.24. This example will be used throughout next chapter to serve as an explanatory example. The objects, both dead and alive, are manifested as three "hot" areas.

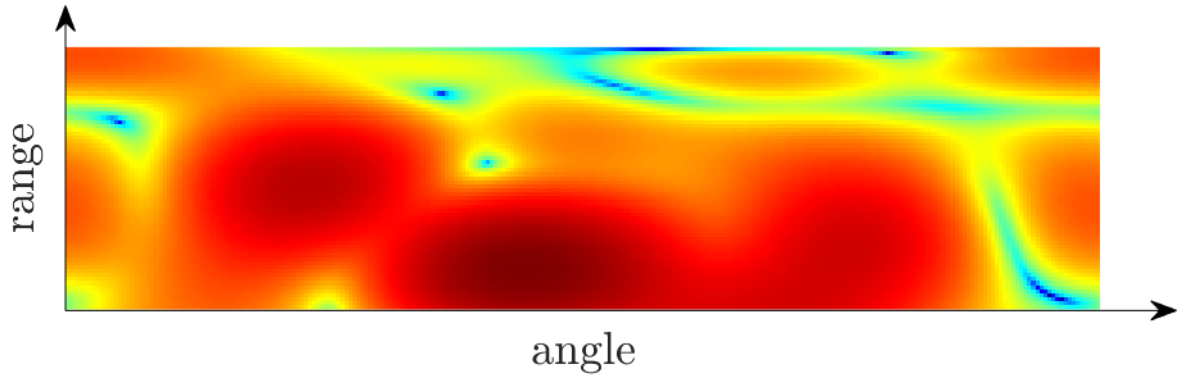

Figure 2.24: Heat map with two subjects and a chair between them.

It can be noticed, that the objects are not easily distinguishable from the surroundings in this heat map, and seem to blend into each other more or less. This is due to both noise and clutter from the surroundings of the objects. The next chapter will demonstrate how objects can be located in this heat map using signal processing techniques.

3 Signal Processing Chain

The previous chapter introduced the basics of the FMCW radar's theory of operation, and the basics of how to obtain the range and angular profiles, as well as the range-angle heat map. This chapter will demonstrate how the radar's raw data can be processed through a signal processing chain whose output is an estimation of the breath and heart rates. This signal processing chain will build up step by step, explaining the importance of each step, until the whole chain is presented

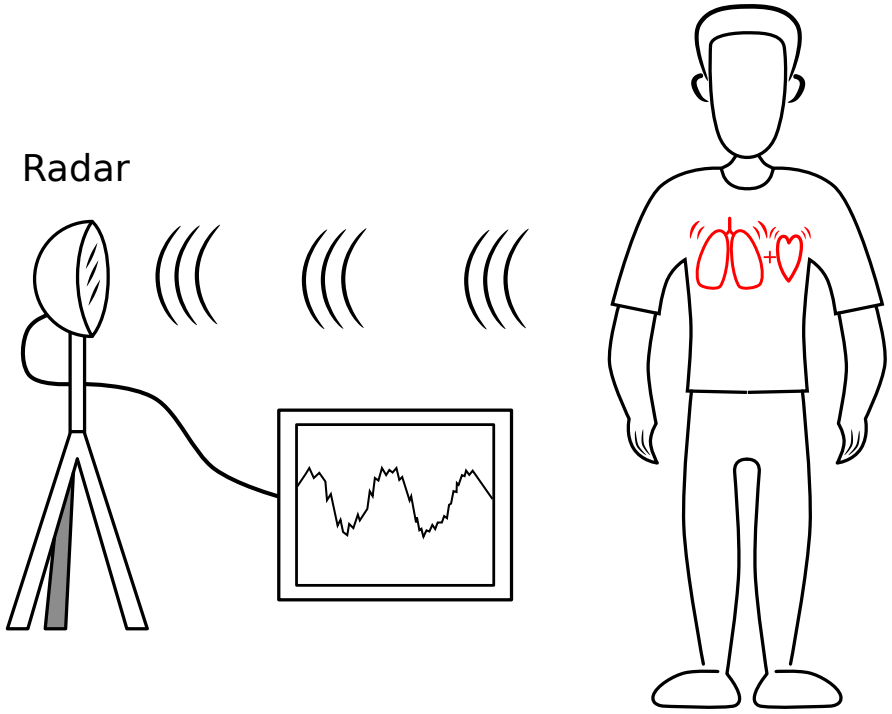

Figure 3.1: The chest wall motion corresponds to a change in phase.

The idea behind using radar to measure the breath and heart rates is as such: the chest wall motion of the subject is modulated by both the breath and heart motions. This chest wall motion although small, is picked up by the radar as a phase variation of the range-angle bin value, since the phase variation is very sensitive to small variations in target range. The analysis of this phase signal then enables the estimation of the breath and heart rates. An illustration of the phase variation due to chest wall motion is shown in Fig. 3.1.

The process on a high level is shown in Fig. 3.2, and starts with obtaining the raw radar data, which was shown in the previous chapter. The next step of the process is to detect where the live targets are in terms of their range-angle bin locations, and to track the phase of those bins. Then, for each detected live target, those phase values are input into the estimation algorithm which estimates the breath and heart rates. This chapter will be split into two sections; one for the tracking step and one for the estimation step.

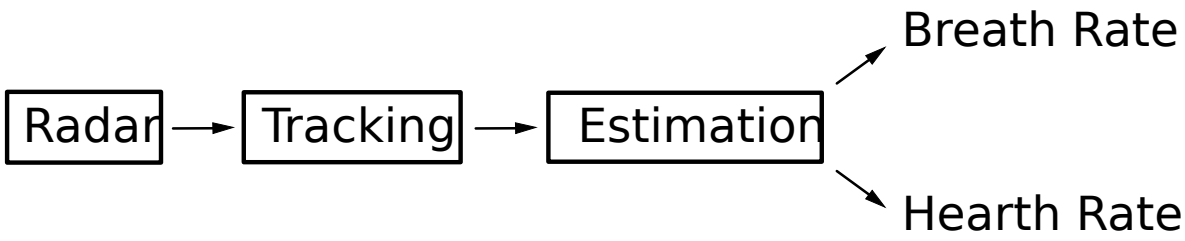

Figure 3.2: A top level view of vital sign estimation.

3.1 Tracking

The tracking step is responsible for locating objects in radar's field of view and determining which objects are likely to be humans and not dead objects, and then tracking the phase variation of live objects. The input to the tracking step is the raw radar data as shown in Fig. 2.20, this consists of a two dimensional matrix with rows as much as the radar has RX antennas, and columns as much as the number of samples taken by the ADC unit per chirp. This input is available to the tracking step every chirp. The output of the tracking step is the phase variation for all the live targets.

The example to be used throughout this chapter will be the same as the one used in last chapter; two persons with a chair in between, with one person sitting and the other standing. The use of this example enables us to test the signal processing chain with our requirements; more than one person, and more than one orientation, while making sure that non-live objects are discarded. To start, each object detected in front of the radar is given and index. Starting from 1 with the right-most object and progressing sequentially as we go to the left. This is shown in Fig. 3.3

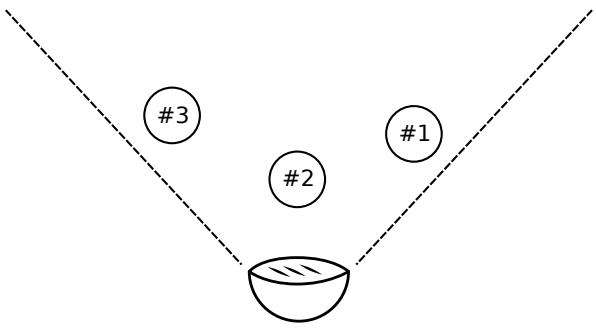

Figure 3.3: Indexing of the targets.

On a high level, tracking is composed of: detection; where we locate the targets' range-angle bin locations, testing; where each detected object is tested as to whether it is live or dead, and then bin monitoring; where we monitor the phase values of the range-angle bin corresponding to live objects. This is illustrated in Fig. 3.4.

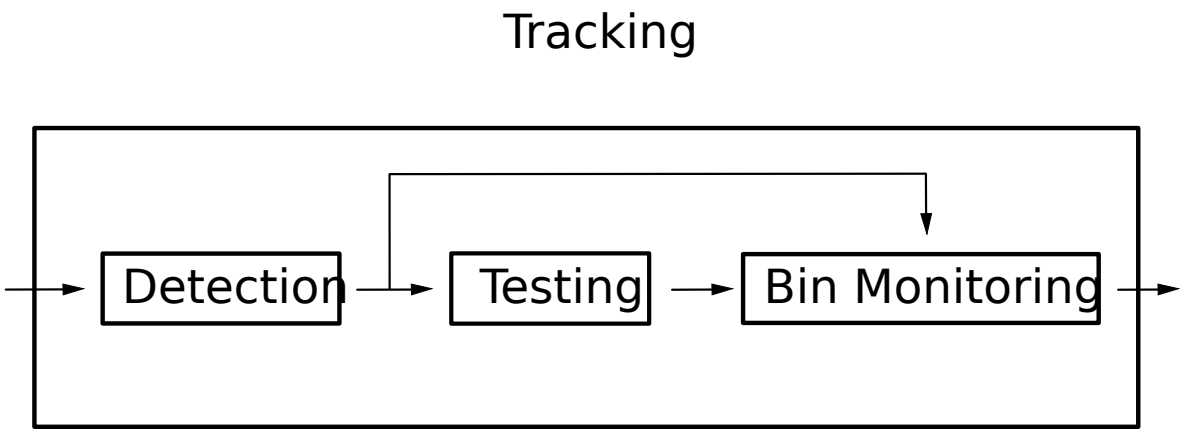

Figure 3.4: A high level view of tracking.

3.1.1 Detection

The steps of detection are shown in Fig. 3.5. The first four steps have already been demonstrated in the previous chapter, and are concerned with obtaining the range-angle heat map, which for this example is as seen in Fig. 2.24. As mentioned, it can be seen that the three objects are not easily distinguishable from the surroundings, and seem to blend into each other. This is the first problem we encounter.

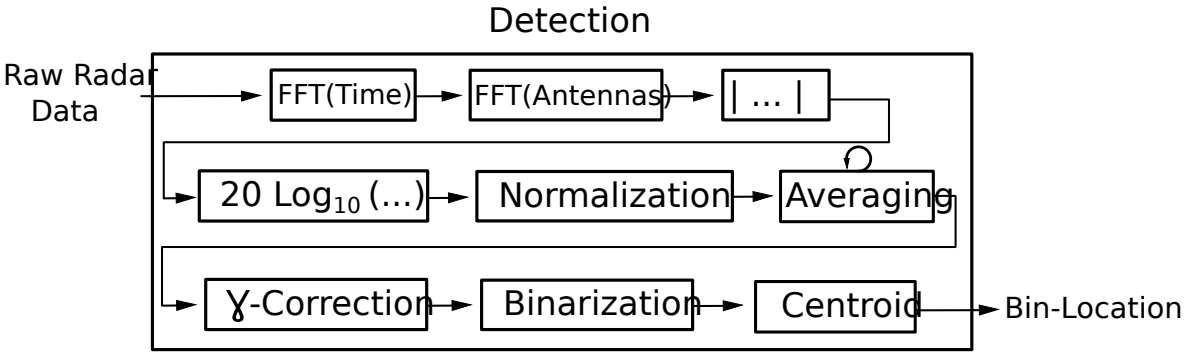

Figure 3.5: The steps involved in detection.

To solve this, we first normalize the heat map, such that highest decibel value is zero. This is achieved by subtracting all the decibel values in the heat map by the maximum value in the heat map using 3.1. Then, any decibel value below $Threshold_{dB}$ is clipped at $Threshold_{dB}$. This results in a normalized and clipped heat maps as shown in Fig. 3.6

$$HeatMap = HeatMap - max(HeatMap) \tag{3.1}$$

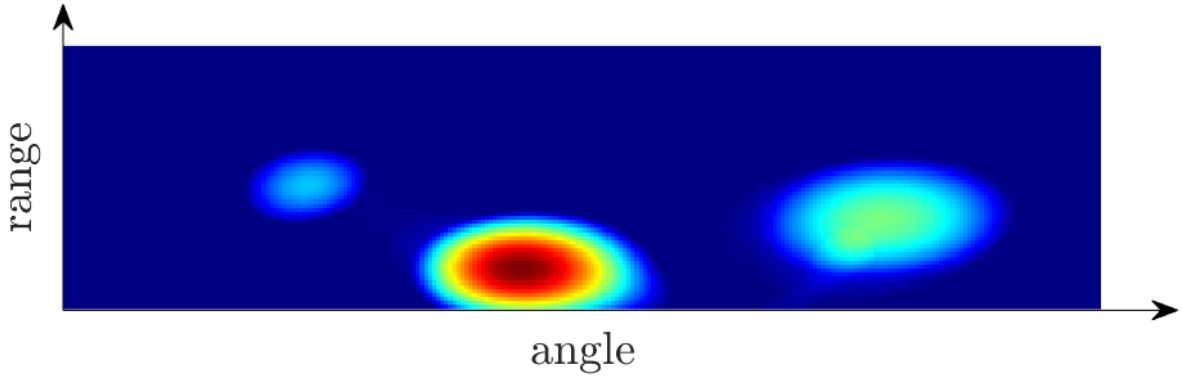

Figure 3.6: The heat map after normalization and clipping.

Now, all three objects can be clearly seen as three distinct hot areas in the heat map. The next problem encountered is that due to noise the heat map is not stable, and the intensity of objects vary significantly between frames from different chirps. For example, the same fame seen in Fig. 3.6 turns into the frame seen in Fig. 3.7 a couple of frames later.

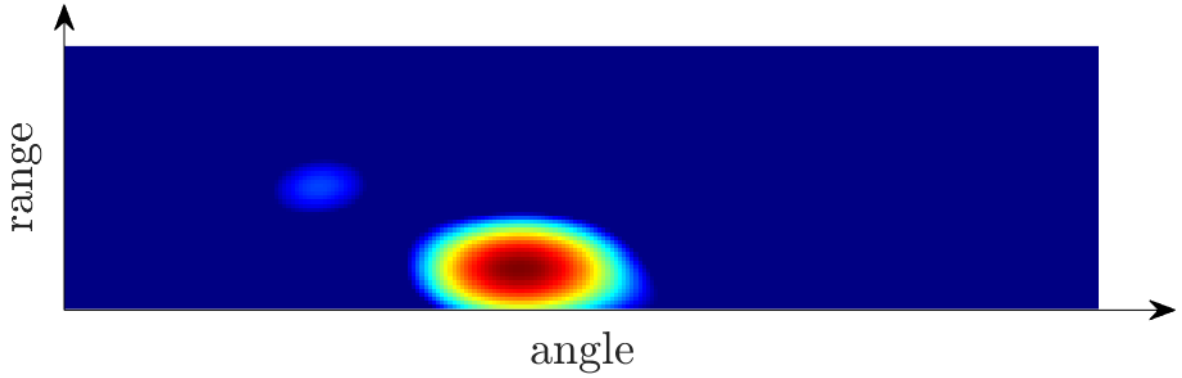

Figure 3.7: The #1 target is not visible a few frames later.

To fix this, we apply weighted averaging between each new heat map and the previous one for all frames within the first T_{detect} seconds. So, given a heat map $HeatMap_{new}$ corresponding to the new heat map calculated after the normalization step, and a previous heat map $HeatMap_{previous}$, we calculate the final heat map $HeatMap$ using

$$HeatMap = (\alpha)HeatMap_{previous} + (1 - \alpha)HeatMap_{new} \tag{3.2}$$

where α is a smoothing factor. Choosing α's value just a little less than 1, like 0.99, gives the heat map stability and all objects are stably manifested in the heat map after T_{detect} seconds. Next, image processing techniques are employed to find the centers of the hot areas found in the heat map, and so we convert our decibel heat map into a gray-scale image, by mapping the decibel values to the range $[0, 1]$ using

$$GrayScale = \frac{HeatMap - min(HeatMap)}{max(HeatMap) - min(HeatMap)} \tag{3.3}$$

The corresponding gray-scale image is shown in Fig. 3.8. Now, to strictly define out the objects, we apply binary thresholding to the gray-scale image. Binary thresholding will set any pixel value above a certain threshold value of $Threshold_{binary}$ to 1.0 (fully bright pixel), otherwise, that pixel shall be set to 0.0 (fully dark pixel). After this operation, we end up with an image as shown in Fig. 3.9.

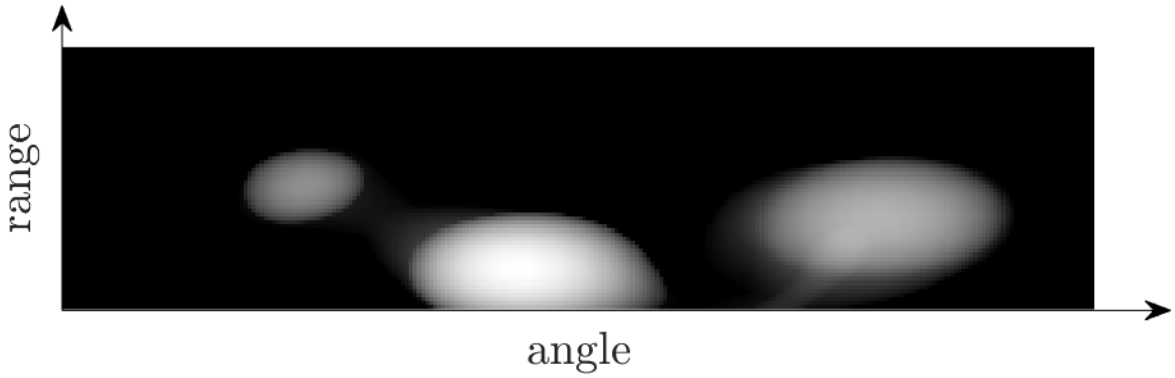

Figure 3.8: Converting the heat map to a gray scale image.

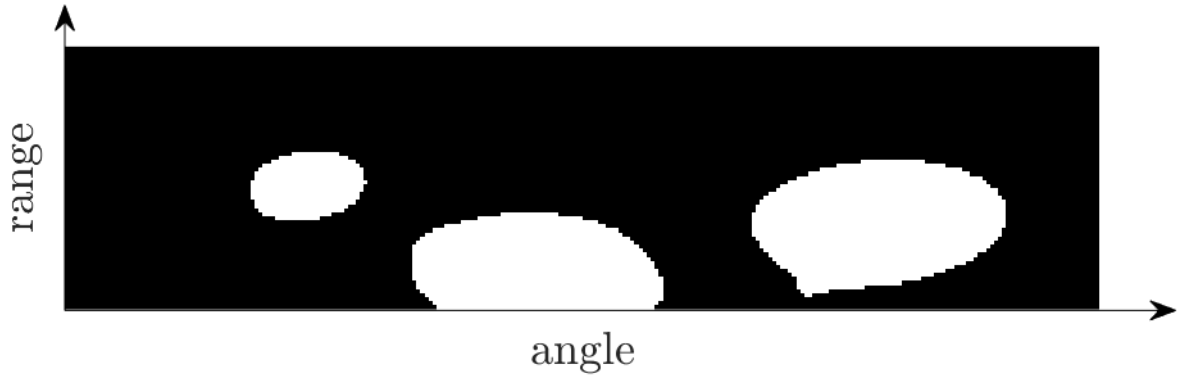

Figure 3.9: Applying binarization the gray-scale image.

There were cases where not all objects would "survive" the binarization step, especially when there is another more prominent object in the frame. One solution to this could be to simply lower the thresholds $Threshold_{dB}$ and/or $Threshold_{binary}$. However, this would create problems in other cases, where it would sometimes cause two close objects to merge into one big blob on the binarized image.

The way around this was to use gamma correction. The idea of gamma correction is to apply the nonlinear function $V_{out} = AV_{in}^{\gamma}$ on each pixel in the gray scale image, where typically $A = 1$ and $\gamma < 1$ are used, which is plotted in Fig. 3.10. As seen, pixels with lower values will get boosted to higher values, while pixels with already high values tend to stay more or less the same. The effect of gamma correction is shown in Fig. 3.11 and Fig. 3.12.

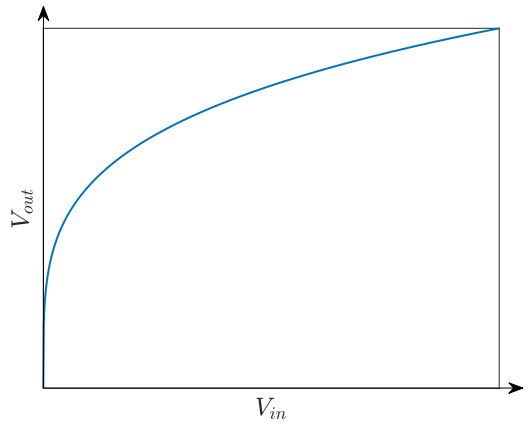

Figure 3.10: Gamma correction has a stronger effect on lower pixel values.

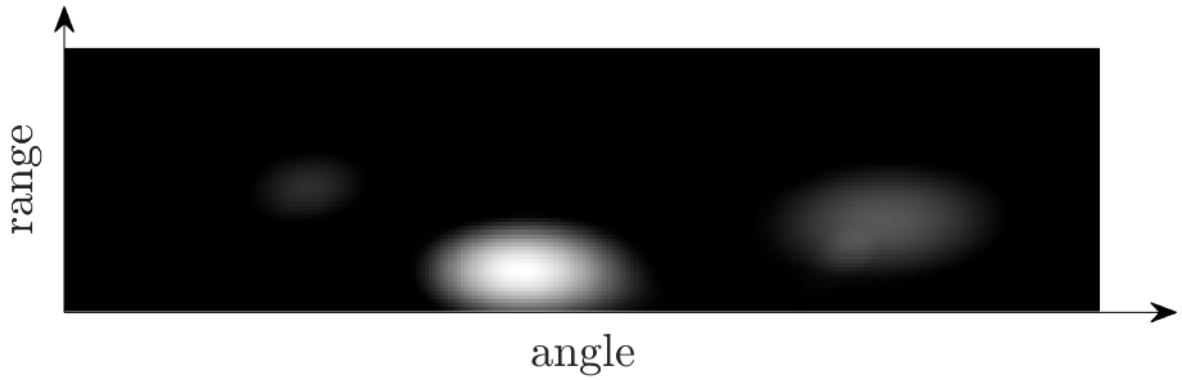

Figure 3.11: Not using gamma correction may cause the #3 target not to get detected.

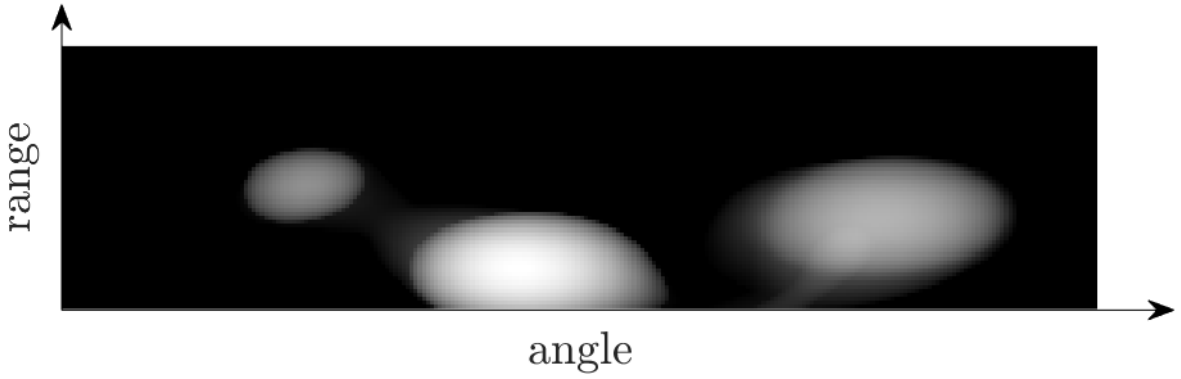

Figure 3.12: Using gamma correction improves the chance of fainter objects to be detected.

After binarization our goal is to detect the centroids of each of the three bodies seen in Fig. 3.9, since those locations are most likely to represent the object locations correctly. The MATLAB® function `bwlabel()` will distinguish between the different fully-connected bodies in the image and label them. This allows us to extract the pixel coordinates of each object in the form $\{(x_1, y_1), (x_2, y_2), (x_3, y_3), \dots\}$, where x_i and y_i are image coordinates. We then obtain the center of each detected object by calculating the centroid coordinates using

$$x_{centroid} = mean(\{x_1, x_2, x_3, \dots\}) \tag{3.4}$$

$$y_{centroid} = mean(\{y_1, y_2, y_3, \dots\}) \tag{3.5}$$

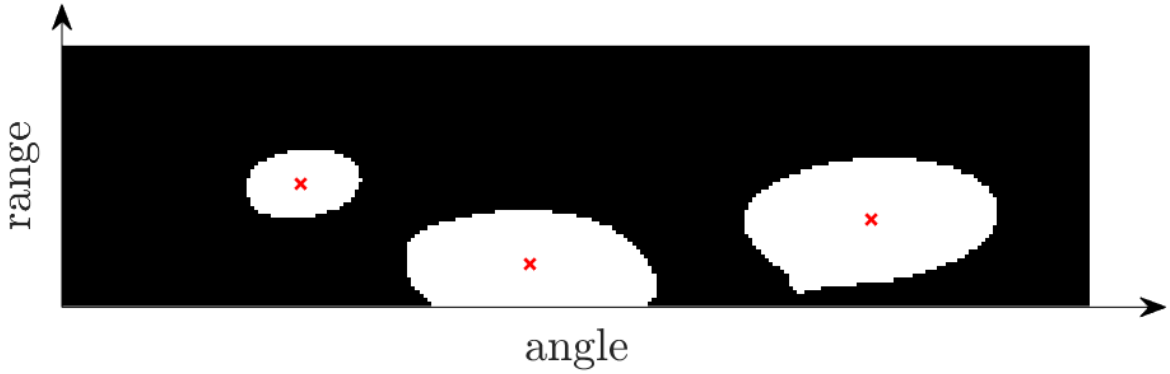

Figure 3.13: The centroid of each body is marked with a red x.

The marked centroids of each body are shown in Fig. 3.13. Now that the centroids have been marked, we have an estimation as to where each object is located, since $x_{centroid}$ and $y_{centroid}$ can be mapped to real world coordinates. We are also able to mark corresponding range-angle bins for monitoring each object's phase variation as shown in Fig. 3.14. Recall that a range-angle bin value is the value of $Y[k, m]$ as introduced last chapter.

Tracking the phase of each marked range-angle bin value over successive chirps as shown in Fig. 3.15 allows us to monitor the phase variation of the object corresponding to this range-angle bin. In turn, this phase variation corresponds to slight range variations. In the case that the monitored object is a live subject facing the radar, then this phase variation will correspond to the small motion corresponding to their chest wall motion, from which their breath and heart rates can be estimated.

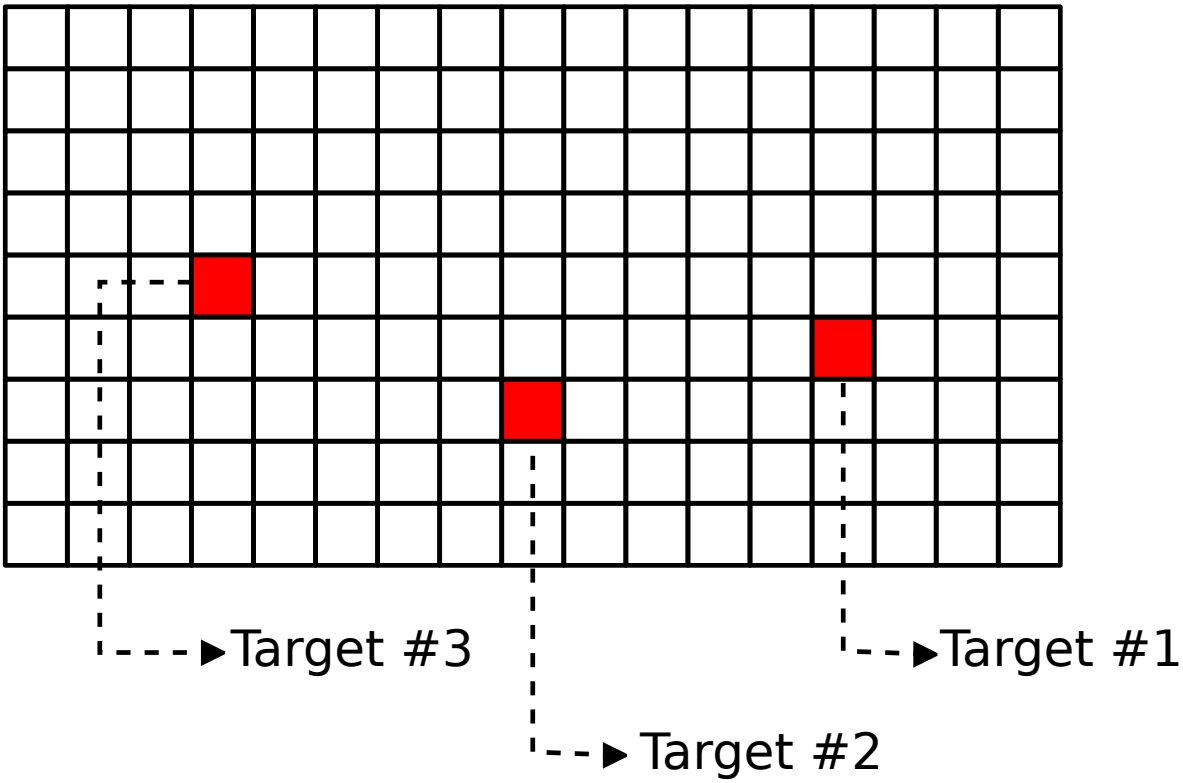

Figure 3.14: Three range-angle bins are marked for monitoring.

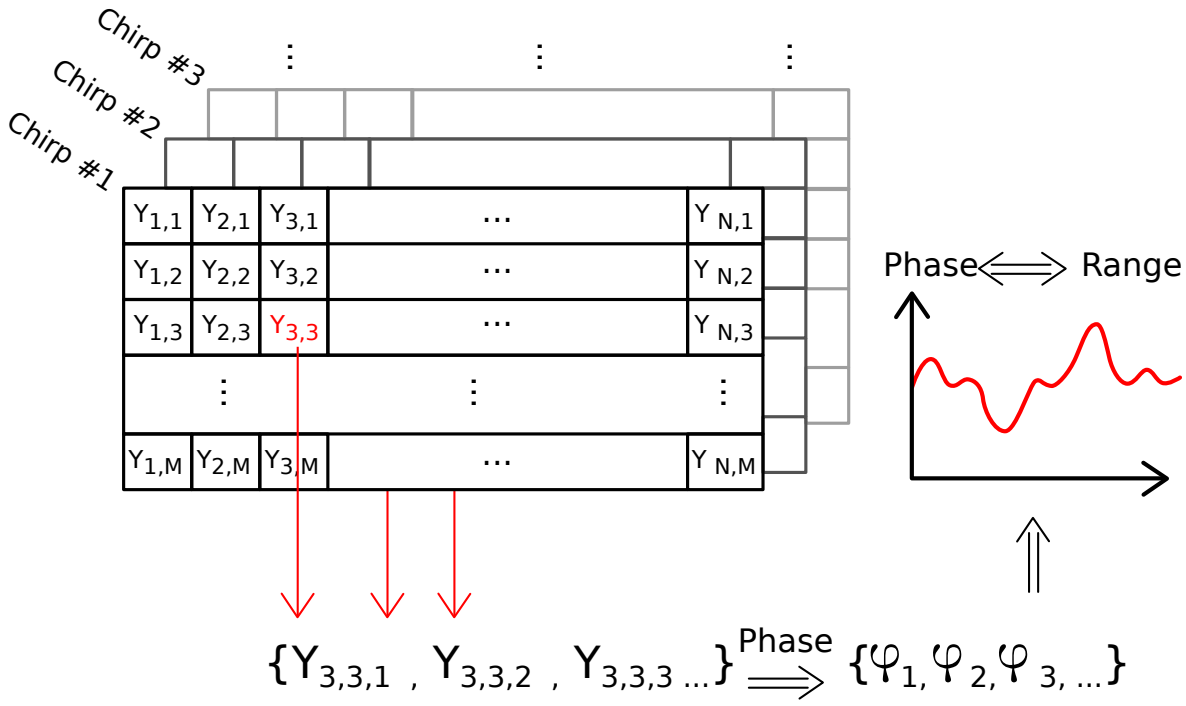

Figure 3.15: Monitoring the phase of a marked range-angle bin across several chirps.

3.1.2 Testing

Now that the range-angle bin for each object has been marked we are able to track objects' phase variations. However, it is not certain that all, or even any, of the detected objects are live subjects. As mentioned, in the particular example being demonstrated there are actually two subjects with a chair in between them. Monitoring that chair's phase variation, and trying to estimate a breath and heart rate from it is not only a waste of computational resources, but also, could lead to confusion when interpreting the results. Therefore, the next phase of the tracking step is to test as to whether each object is live, or not.

To do this, we record the phase values of each object for T_{test} seconds after the detection phase is complete. Let $\phi_{i,j}$ be the jth phase value recorded for the ith object during the testing phase, during which we'll collect N_{test} phase values per object. Then after T_{test} seconds since the start of the testing phase we'll have recorded the phase values $\{\phi_{i,1}, \phi_{i,2}, \phi_{i,3}, \ldots \phi_{i,N_{test}}\}$ for the ith object. Next, we calculate per object the variance of the collected phase values as:

$$\sigma_i^2 = var(\{\phi_{i,1}, \phi_{i,2}, \phi_{i,3}, \ldots, \phi_{i,N_{test}}\}) \tag{3.6}$$

An object which represents a live subject will have a much higher phase variance value than a dead object, and so if an object i's phase variance passes a certain threshold $Threshold_{\sigma^2}$, then this object may be considered a live subject, otherwise it is considered dead, and its range-angle bin values are ignored. This is the case with the #2 object as shown in Fig. 3.16.

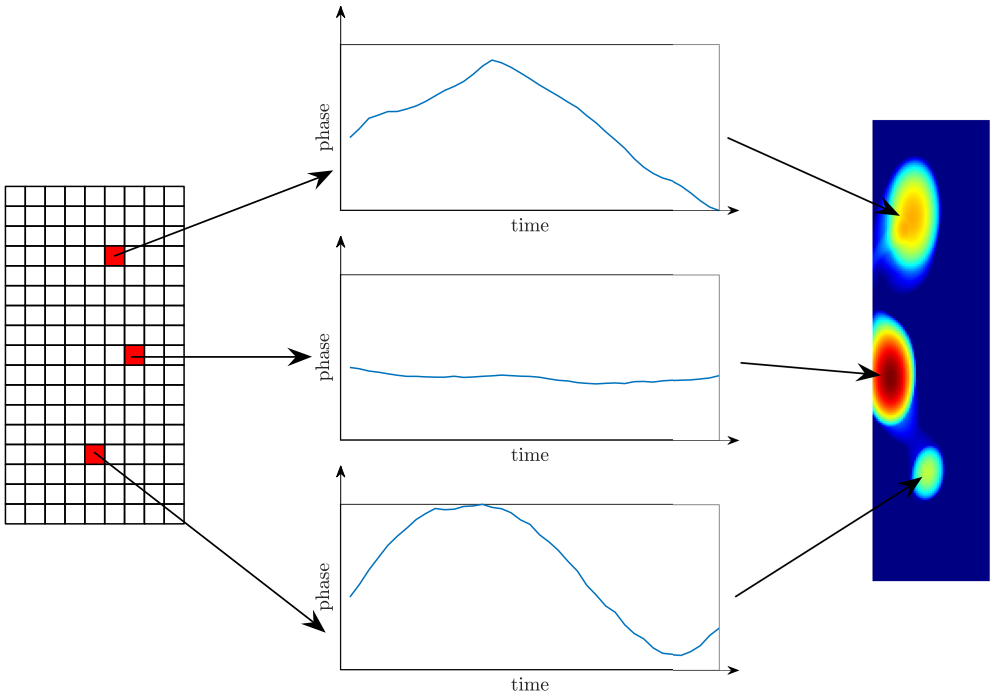

Figure 3.16: The #2 object has very little phase variation and so can be assumed dead.

3.1.3 Bin Monitoring

After we have detected where objects are located, as well as tested which objects correspond to live subjects, we can monitor the marked range-angle bin's phase variation over extended periods of time. As seen in the example in Fig. 3.17, only the phases of the #1 and the #3 objects are monitored, since the #2 object did not pass the testing phase.

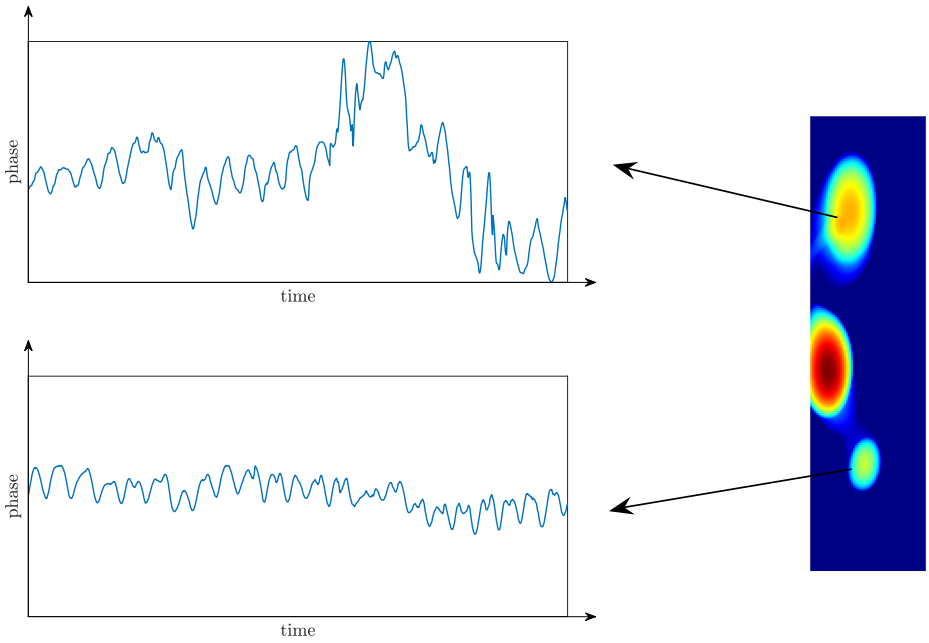

Figure 3.17: Monitoring the phase variation of the #1 (top) object and the #3 (bottom) object.

The clearest component in both phase variation plots is the breath-related phase variation, which can be seen as an almost-sinusoidal form throughout the whole plot. The heart-related phase variation is less obvious, but is still there, and could be seen a few times in the #3 subject's phase variation as slight nudges in some of the peaks. The #1 object corresponds to a standing subject, and so the phase variation is noticeably higher than that of the #3 object, which corresponds to a more stable sitting person. The higher variation seen in the #1 object's phase variation is due to random body motion attributed to standing, which blends with the breath and heart-related phase variations.

3.2 Estimation

The next step after tracking is the estimation step, where we use the phase values of each detected live subject to estimate the breath and the heart rates. The estimation step is only able to start after $T_{detect} + T_{test}$ seconds, after which we have a flow of phase values with each chirp, which represent live subjects. The steps of estimation are shown in Fig. 3.18.

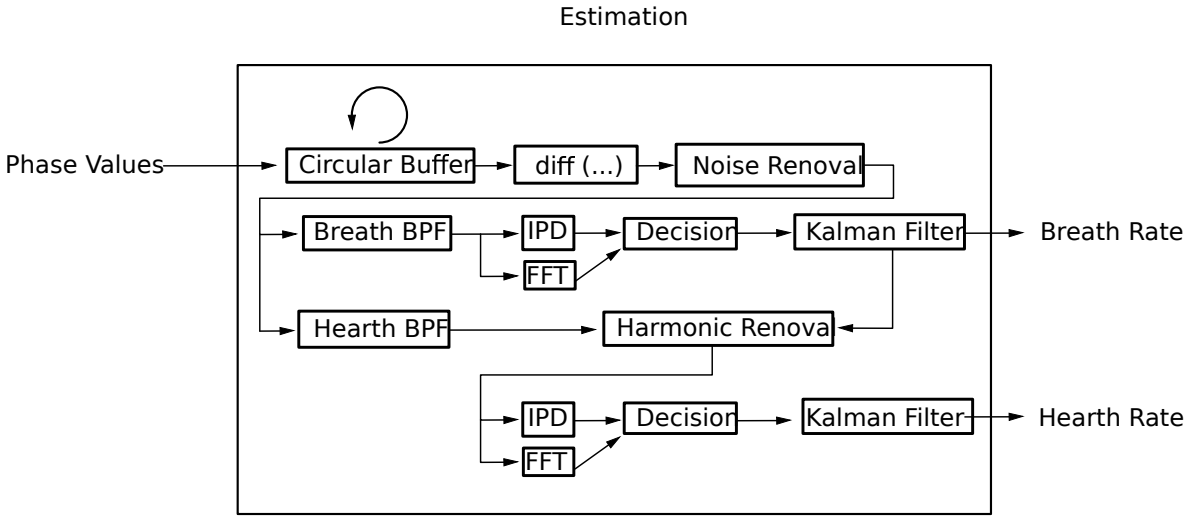

Figure 3.18: The steps involved in estimation.

3.2.1 Circular Buffering

The phase values seen in Fig. 3.17 are actually observed for 60 seconds. Technically, speaking those phase values could be used, but we have two issues. Firstly, we would need to wait for 60 seconds before we could give out our first estimates, which is a long time, and we would have to wait yet another minute for the next estimate, and so on. Secondly, giving out an estimate from 60 seconds worth of phase data correspondingly will average out breath and heart rate variations within those 60 seconds to one reading of breath and heart rate respectively, which may hide significant changes in the vital signs seen during this one minute (such as a patient suddenly starting to hyper-ventilate).

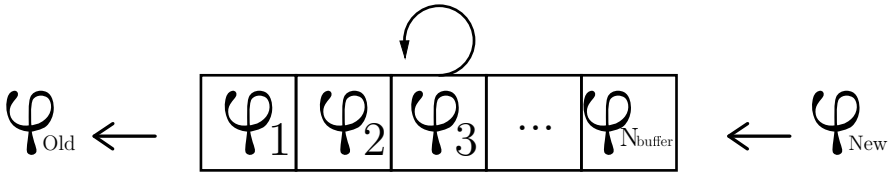

Figure 3.19: Operation of the circular buffer.

The better way to handle this is through a circular buffer approach, where the newest phase value is pushed into the circular buffer from one end, and the oldest phase value is pushed out at the same time. The length of this buffer would correspond to the buffer time capacity of T_{buffer} seconds, and correspondingly would have a length of N_{buffer}. The phase values contained in this buffer would then be used for the estimation of both the breath and heart rates, and so any estimation at any given time would be made using the past T_{buffer} seconds worth of phase values. This operation is shown in Fig. 3.19. The buffer starts out empty, and the algorithm does not output any values until the buffer is full, therefore the first vital sign estimate can only be made after $T_{detect} + T_{test} + T_{buffer}$ seconds. A buffer's worth of phase values from the #3 subject is shown in Fig. 3.20, this window of phase values will be used as the running example for the remainder of the chapter.

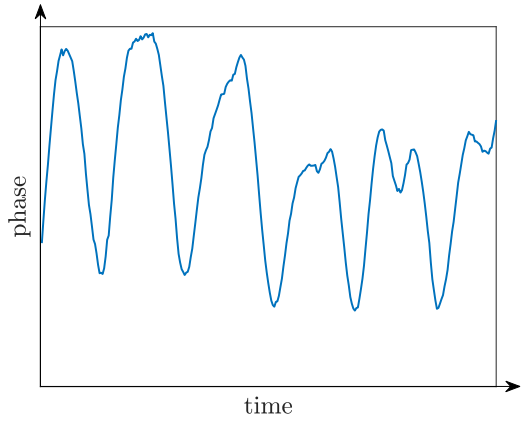

Figure 3.20: A buffer's worth of phase values for the #3 subject.

3.2.2 Noise Removal

This section is concerned with both the **diff(...)** and the **Noise Removal** blocks seen in Fig. 3.18. In the **diff(...)** block we compute the phase differences between the successive phases which helps in removing drifts in phase and in suppressing the breath harmonics [30], which could affect the heart rate estimation. This is achieved using the MATLAB® function `diff(...)` which calculates

$$diff(\{\phi_1, \phi_2, \phi_3, \ldots, \phi_{N_{buffer}}\}) = \{(\phi_2 - \phi_1), (\phi_3 - \phi_2), \ldots, (\phi_{N_{buffer}} - \phi_{N_{buffer}-1})\} \tag{3.7}$$

which can be written as

$$\{\Delta\phi_1, \Delta\phi_2, \Delta\phi_3, \ldots, \Delta\phi_{N_{buffer}-1}\} \tag{3.8}$$

The differential phase might be corrupted by several noise-induced phase wrapping errors especially if the phase values are close to $-\pi$ or π [30], to solve this we apply the **Noise Removal** block, where we compute a forward and backward difference for each value of $\Delta\phi_i$; $(\Delta\phi_i - \Delta\phi_{i+1})$ and $(\Delta\phi_i - \Delta\phi_{i-1})$ respectively. If either the forward or backward difference of $\Delta\phi_i$ exceeds a certain threshold $Threshold_{noise}$, then we replace $\Delta\phi_i$ by $(\Delta\phi_{i+1} + \Delta\phi_{i-1})/2$. In Fig. 3.21 the result after the **diff(...)** and the **Noise Removal** blocks is shown.

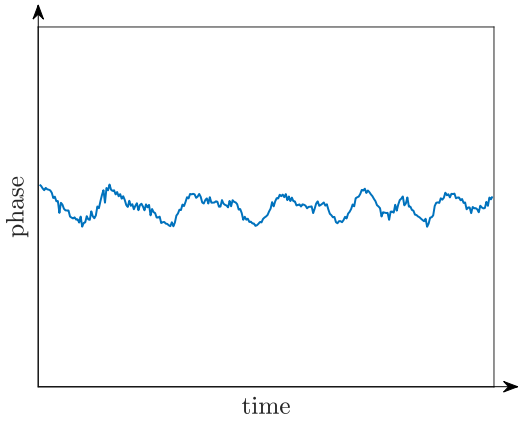

Figure 3.21: The differential phase after noise removal.

3.2.3 Bandpass Filtering

The plot shown shown in Fig. 3.21 has little resemblance to a breathing pattern, and none to that of a heart beat pattern. This is where the **bandpass filtering** block comes in. The basis of using bandpass filtering is the fact that the breath and heart rate spectrum occupy non-overlapping frequency ranges. So we can use two bandpass filters, one for the breath and one for the heart rate, in order to extract the corresponding waveform. Each bandpass filter uses cutoff frequencies corresponding to the respective vital sign's typical frequency range. The bandpass filters' outputs are shown in Fig. 3.22 and Fig. 3.23, where the breath and the heart wave forms, respectively, are much clearly visible.

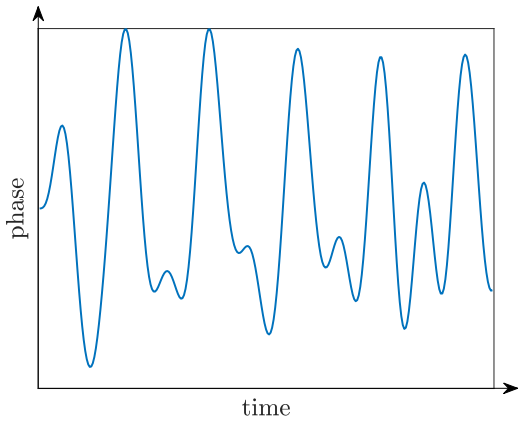

Figure 3.22: The breath waveform.

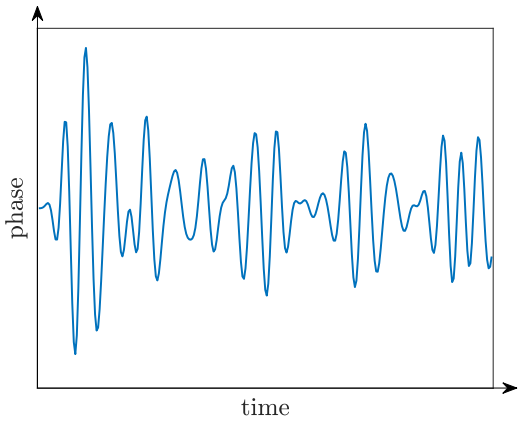

Figure 3.23: The heart waveform.

3.2.4 IPD Estimation

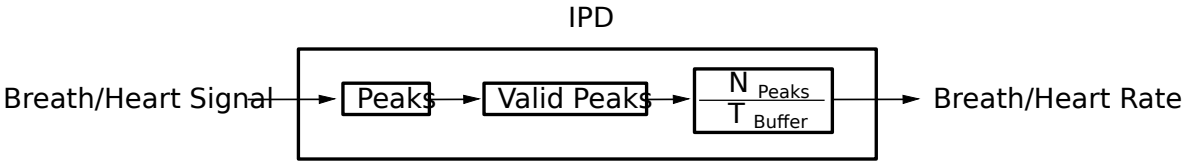

Figure 3.24: Steps for the IPD estimation method.

Now that we have the breath and heart waveforms, we are able to start estimating the respective rates. The simplest method of doing so is the Inter-Peak Distance (IPD) estimation method. IPD works by smartly counting peaks found in the waveform, then using this count to estimate the corresponding rate. First, we find the peaks in the signal using the MATLAB® function `findpeaks(...)`, and only retain positive-valued peaks. A minimum inter-peak distance value P_{min} is calculated from the maximum frequency expected for the respective rate, breath or heart, using

$$P_{min} = \frac{1}{f_{maximum}} \tag{3.9}$$

the frequency $f_{maximum}$ is taken to be the same value as the upper cutoff frequency from the respective rate's bandpass filter. The first positive-valued peak is counted as a valid peak. The next valid peak is chosen such that the distance between it and the previous peak is greater than or equal to P_{min}. This is repeated until all the valid peaks in the signal are counted. The valid peaks in our example are shown in Fig. 3.25 and Fig. 3.26. If the number of valid peaks counted is N_{peaks}, then the respective rate can then be calculated using:

$$f_{IPD} = \frac{N_{peaks}}{T_{buffer}} \tag{3.10}$$

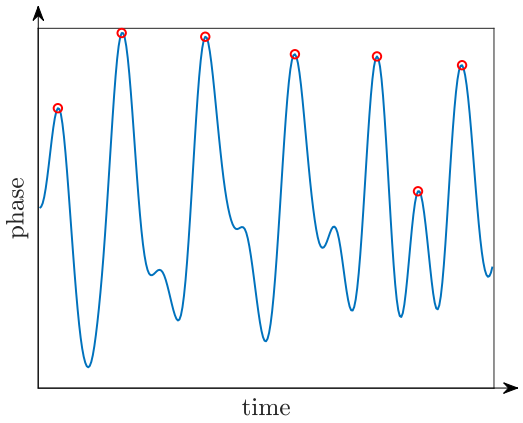

Figure 3.25: The valid peaks of the breath waveform.

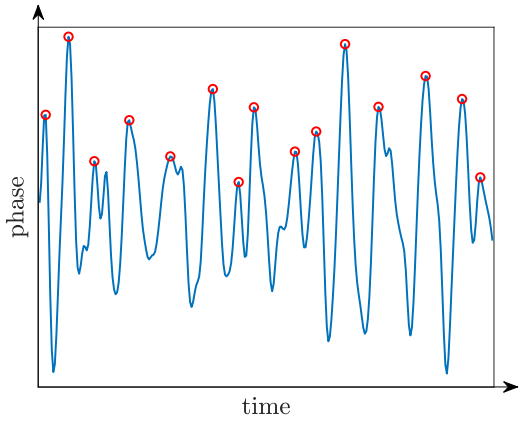

Figure 3.26: The valid peaks of the heart waveform.

3.2.5 FFT Estimation

The FFT method is largely based on using the Fast Fourier Transform, and hence the name, and like the IPD method, it is also used to estimate breath and heart rates given the breath and heart waveforms, respectively. However, unlike the IPD method which is the exact same for both breath and heart rate estimations FFT method has different definitions depending on whether the breath or the heart rate is being estimated, nevertheless, both variants have a commonality in their definitions, which shall be explained first before specializing for each vital sign.

The first step for both variants is to apply the FFT on the respective waveform, breath or heart, and plot amplitude vs. frequency to obtain a frequency spectrum, as shown in Fig. 3.27 and Fig. 3.28. This frequency spectrum is an indicator as to which frequencies are more prominent in the respective waveform, breath or heart. Ideally, the frequency corresponding to the maximum amplitude would correspond to the respective vital sign rate. However, this is not the case most of the time, since the breath and heart waveforms are not purely sinusoidal, and have different frequency components mixed in.

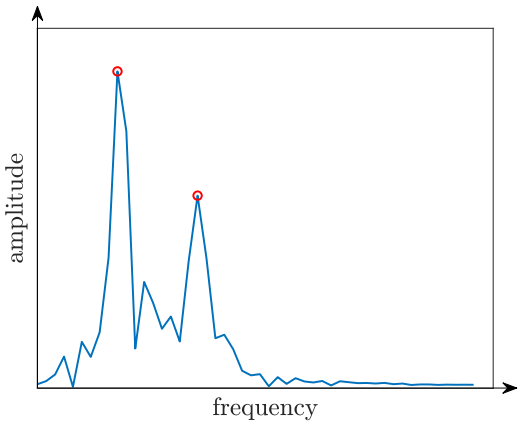

Figure 3.27: Breath frequency spectrum with top two frequencies marked.

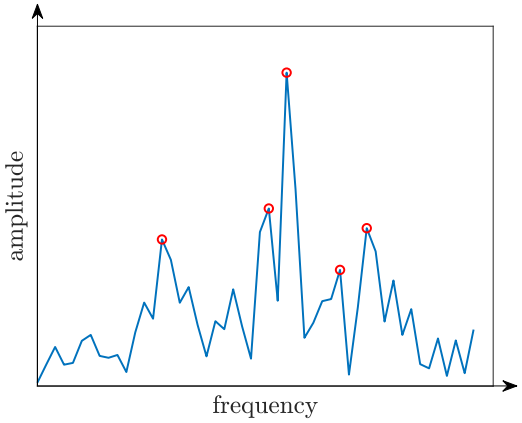

Figure 3.28: Heart frequency spectrum with top five frequencies marked.

So, instead of only choosing the frequency that corresponds to the maximum amplitude, we choose the frequencies that correspond to the top N_{top} amplitudes, where N_{top} is generally different for both the breath and heart rate estimations. Then, for each of those N_{top} peaks we calculate a base confidence metric $BaseConfidence_j$, where j is the peak index, ranging from 1 to N_{top}. The value of $BaseConfidence_j$ is calculated as the ratio of the amplitude of peak j added to the amplitudes of the N_{side} frequency bins on both sides of the peak, over the sum of the amplitudes of the remaining frequency bins in the typical frequency range of the corresponding vital sign [30]. Here this typical frequency range is chosen to match the cutoff frequencies of the corresponding vital sign's bandpass filter.

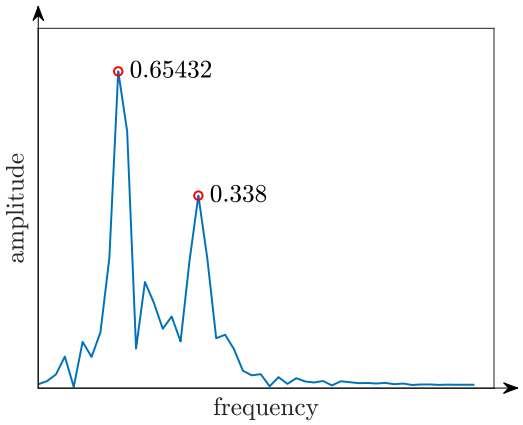

Figure 3.29: Base confidence scores for the top breath frequencies.

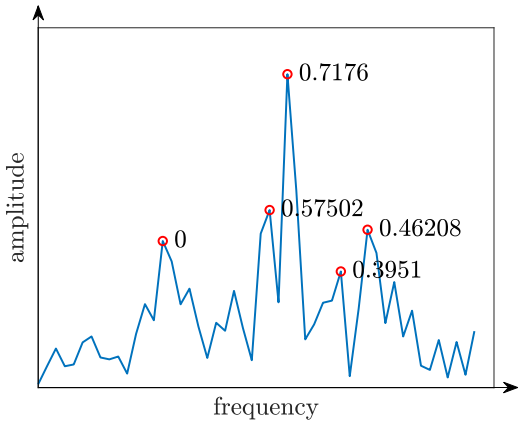

Figure 3.30: Base confidence scores for the top heart frequencies.

The confidence score is a measurement of how likely the FFT estimate is to be correct and close to the correct value of the vital sign rate. The calculated base confidence scores for our example are shown in Fig. 3.29 and Fig. 3.30. In Fig. 3.30, a peak with 0 base confidence score can be seen, this is a result of the corresponding peak frequency lying outside the typical frequency range for the respective vital sign.

Breath Variant

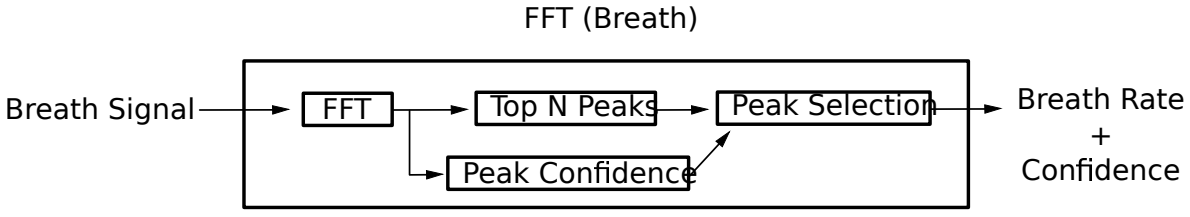

Figure 3.31: Steps for the FFT method breath variant.

Proceeding to estimate the breath rate estimation, we first calculate the final confidence score $Confidence_j$ for the jth peak corresponding to frequency f_j as:

$$Confidence_j = \frac{BaseConfidence_j}{f_j^2} \tag{3.11}$$

We then choose the frequency with the highest final confidence score as the breath rate estimate by the FFT method $f_{Breath,FFT}$, with its corresponding confidence score $Confidence_{Breath,FFT}$, which shall be used again later on.

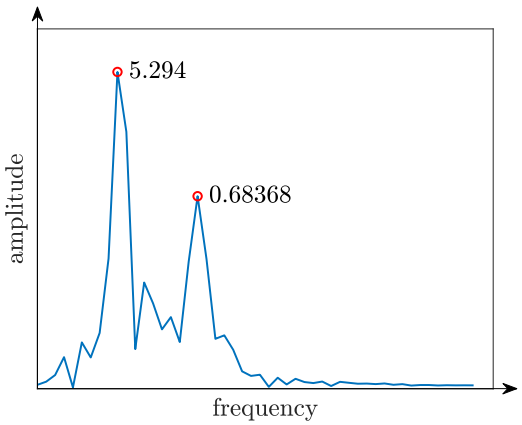

Figure 3.32: Final confidence scores for the top breath frequencies.

The choice 3.11 was found to make the correct breath rate correspond to the frequency with the highest confidence rate most of the time, and gave the best results, by giving preference to lower frequency values. In the example shown in Fig. 3.32 the highest peak does correspond to the highest confidence rate, however this is not always the case as indicated in Fig. 3.33.

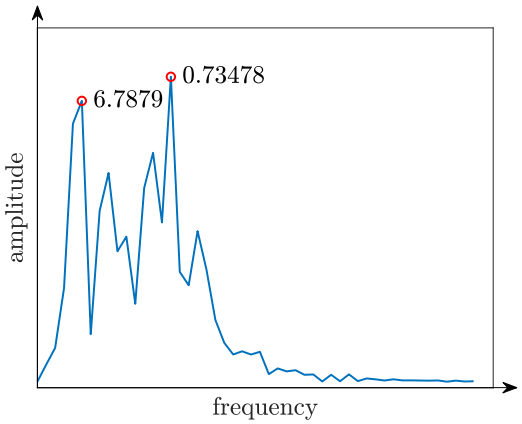

Figure 3.33: The highest peak does not always correspond the highest confidence rate.

Heart Variant

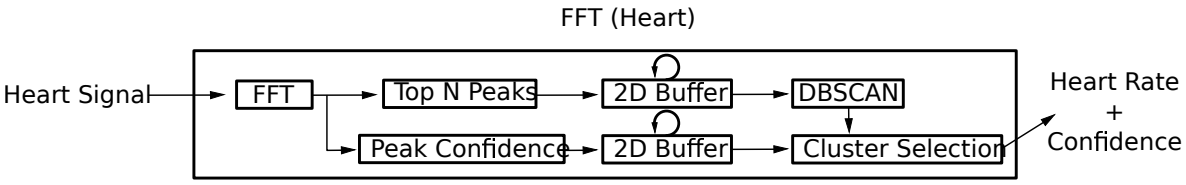

Figure 3.34: Steps for the FFT method heart variant.

Proceeding with the heart rate estimation, we use a density based approach based on the approach used in [30]. As with the breath rate estimation, we start with the top N_{top} frequencies $\{f_1, f_2, \ldots, f_{N_{top}}\}$, and their corresponding base confidence scores $\{BaseConfidence_1, BaseConfidence_2, \ldots, BaseConfidence_{N_{top}}\}$. The N_{top} frequencies are then placed in a circular buffer that accumulates the top frequencies of the past $T_{density}$ seconds at any given time. This buffer has N_{top} rows, and $N_{density}$ columns. This is depicted in Fig. 3.35.

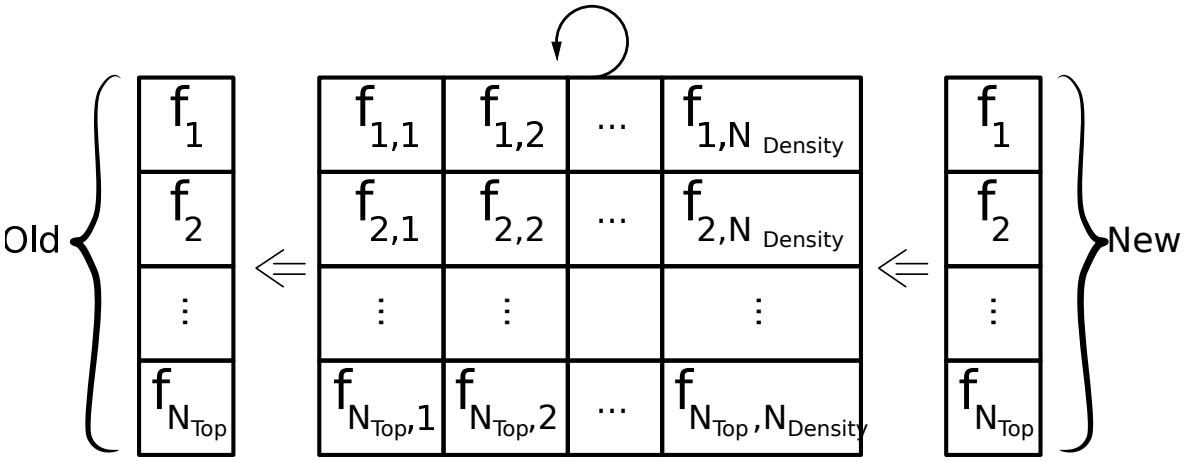

Figure 3.35: Buffering the top N_{top} frequencies over time.

The corresponding base confidences are buffered in the same way in a N_{top}x$N_{density}$ dimensional buffer. As soon as the buffer is full, we can start estimating the heart rate. Meaning that the first heart rate estimate using the FFT method is estimated $T_{detect} + T_{test} + T_{buffer} + T_{density}$ seconds after the algorithm starts. Proceeding, the 2D frequency buffer is converted to a 1D buffer, and the its contained frequencies are clustered according to the Density-Based Spatial Clustering of Applications with Noise (DBSCAN) algorithm, which partitions the frequencies into clusters depending on how close they are to each other. The base confidences from the 2D base confidence buffer are clustered according to how the corresponding frequencies are clustered.

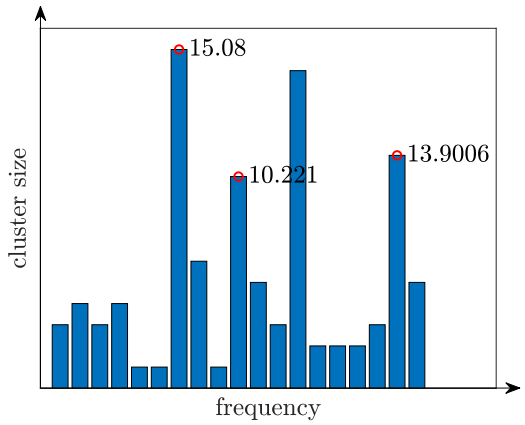

Figure 3.36: Cluster size vs. cluster frequency with the top 3 cluster confidences noted.

Each frequency cluster i will have a cluster size $ClusterSize_i$, a cluster frequency $ClusterFrequency_i$, a base cluster confidence $BaseClusterConfidence_i$, and final cluster confidence $ClusterConfidence_i$. The value of $ClusterFrequency_i$ is calculated as the median value of the frequencies present in the ith cluster, and the value of $BaseClusterConfidence_i$ is calculated as the median of the base confidence scores present in the respective base confidence score cluster. The final cluster confidence $ClusterConfidence_i$ is calculated by:

$$ClusterConfidence_i = (BaseClusterConfidence_i)(ClusterSize_i)(ClusterFrequency_i)^2 \tag{3.12}$$

The calculation of $ClusterConfidence_i$ takes into account the cluster size $ClusterSize_i$, since larger clusters are more indicative of a persistent and correct frequency; and the cluster frequency $ClusterFrequency_i$, giving preference to higher frequencies, which were found to be closer to the correct heart rate most of the time. The frequency clusters of our example are shown in Fig. 3.36, with the clusters of the top 3 final cluster confidences marked. Note that the second largest cluster doesn't make it to the top 3 clusters in terms of final cluster confidence, since the calculation does not depend solely on the cluster size $ClusterSize_i$.

After all the final cluster confidences have been calculated, the value of $ClusterFrequency_i$ corresponding to the highest value of $ClusterConfidence_i$ is chosen as the heart rate estimate by the FFT method $f_{Heart,FFT}$, with corresponding confidence score $Confidence_{Heart,FFT}$ equal $ClusterConfidence_i$.

3.2.6 Confidence-Based Choice

For each of the breath and heart rates, an estimate using each of the IPD and FFT methods will be calculated, along with final confidence scores for the FFT methods' estimates. The final vital sign estimate is assigned based on the final confidence score $ConfidenceScore$, where if it passes a certain threshold $Threshold_{confidence}$, then the FFT method's output f_{FFT} is chosen, otherwise the IPD method's output f_{IPD} is chosen. This is done for both the breath and heart rates. Note that $Threshold_{confidence}$ is generally different for each vital sign. It was found that a correctly tuned value of $Threshold_{confidence}$ results in a final accuracy much better than solely using either f_{IPD} or f_{FFT} alone, for either of the vital signs.

3.2.7 Kalman Filtering

The breath and heart rate estimates after confidence-based selection are shown in Fig. 3.37, along with the reference (ground truth) rates, where it can be seen that both vital sign estimates jitter around the correct reference value. To fix this, one dimensional Kalman filtering [33] is applied to each vital sign estimate.

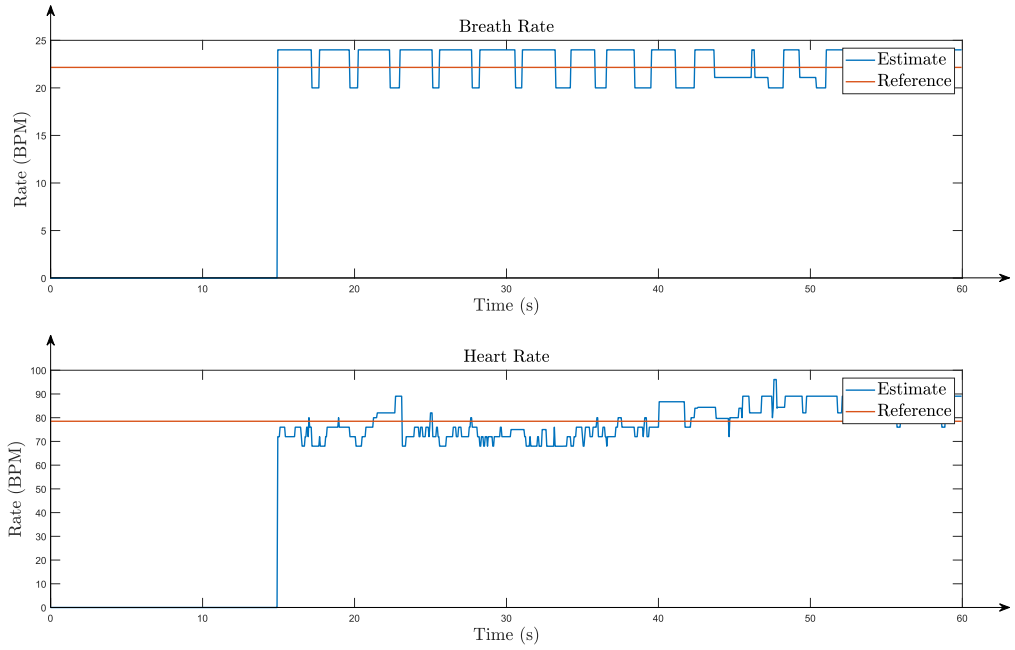

Figure 3.37: The unfiltered breath and heart rate estimates.

A Kalman filter is fed in a series of measurements, typically from sensors but in this case (estimates) from an algorithm, which may contain noise and other inaccuracies, to generate a more reliable and stable estimate. The algorithm is a two-step process that repeats itself iteratively: a prediction step followed by a correction step. In the prediction step a prediction of the variable being measured (estimated) is made, f_{breath} or f_{heart} in this case; in the correction step the noisy measurement (estimate) is used to correct the prediction and give a more reliable estimate with each iteration. Kalman filtering is no simple topic, and explaining it fully and formally is outside the scope of this thesis, however, it shall be explained simply and only as it pertains to this application.

The variables used in the 1D Kalman filter are: $f_{measurement}$, the unfiltered breath or heart rate given by the confidence-based decision block; $f_{prediction}$, the predicted state of the breath or heart rate; $f_{estimate}$, the Kalman-filtered breath or heart rate; p the estimate variance; q, the process variance; and r, the measurement variance. The estimate variance p measures how inaccurate our estimate is, and goes down with each iteration. The process variance q measures how much we believe the true system deviates from our assumed system, which is a constant breath and heart rate assumption, since breath and heart rate are generally slow-varying, but not constant. The measurement variance r measures how inaccurate our measurement (estimate) is; a measurement of how jittery the algorithm is in this case. The

The values of $f_{estimate}$ and p will change with each iteration; with $f_{estimate}$ getting closer to the true respective vital sign rate, and p will approach zero since we expect our estimate to get less erroneous with each iteration. The values of q and r will not change with iterations.

An initial value for $f_{estimate}$ is chosen to be zero, but will approach the true value after a couple of iterations. The initial value of p is chosen to represent how erroneous the initial value for $f_{estimate}$ is, this will cause $f_{estimate}$ to approach the true value more quickly, by making the algorithm aware that it's not reliable (we don't expect the breath and heart rates to be zero). We choose q to represent how erroneous we believe our system model to be, which assumes constant breath and heart rate. For example, someone breathing at 20 BPM will be expected to still be breathing at 20 BPM a couple of seconds later, but over longer periods of time a change is indeed expected, and so q will capture this. Finally, the value of r is chosen to capture how noisy and jittery the algorithm is, and so makes the Kalman filter more resistant to sudden jumps in the vital sign rates estimates. Note that each of the breath and heart rates will have its own Kalman filter with its own generally-different variables.

We start with the prediction step assuming constant breath and heart rate, and so the prediction will be the same as the last estimate, therefore we say that

$$f_{prediction} = f_{estimate} \tag{3.13}$$

In the first iteration $f_{prediction}$ is assigned a value of zero. Then, we update the estimate variance p from the previous estimate variance $p_{previous}$ and the process variance q using

$$p = p_{previous} + q \tag{3.14}$$

In the first iteration $p_{previous}$ is the initial value of p. Next, the Kalman gain K is calculated from the estimate variance p and the measurement variance r using

$$K = \frac{p}{p + r} \tag{3.15}$$

For the correction step, the estimate $f_{estimate}$ is calculated using the prediction $f_{prediction}$, the Kalman gain K, and the measurement $f_{measurement}$ using

$$f_{estimate} = f_{prediction} + K(f_{measurement} - f_{prediction}) \tag{3.16}$$

Finally, the estimate variance is updated again using the previous estimate variance $p_{previous}$ and the Kalman gain K

$$p = p_{previous}(1 - K) \tag{3.17}$$

The steps from 3.13 until 3.17 are repeated with every new breath or heart rate rate given by the confidence-based selection block. With iterations, the value of $f_{estimate}$ approaches the true value, and smooths out the jitter seen in $f_{measurement}$, this is seen in Fig. 3.38

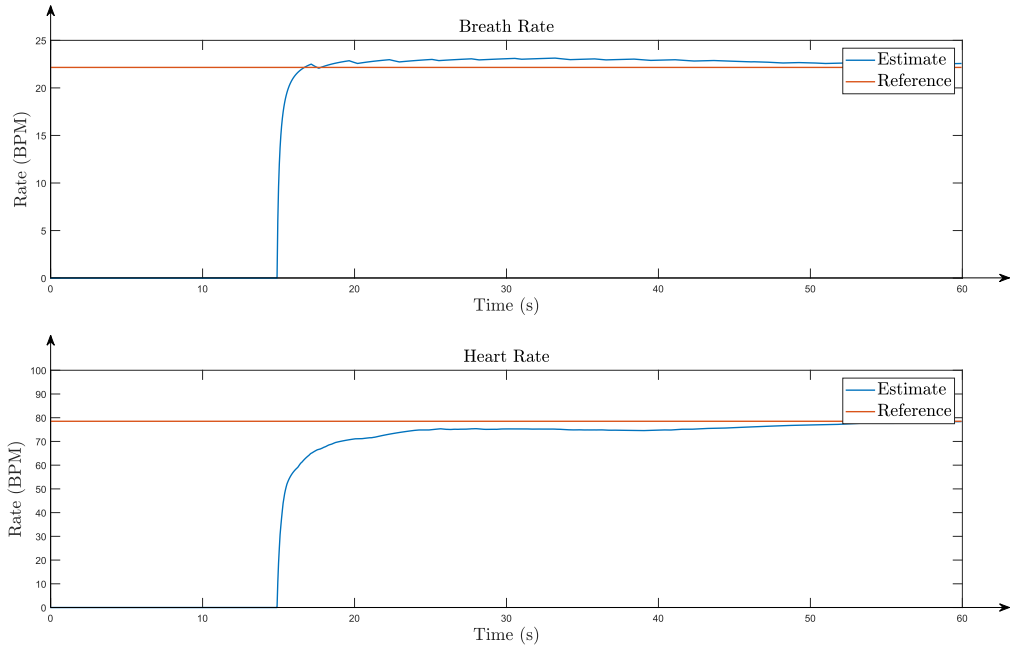

Figure 3.38: The Kalman-filtered breath and heart rate estimates.

3.2.8 Harmonic Removal

Being comparatively higher in signal power compared to the heart waveform, the breathing waveform will still manifest as harmonics in the heart's frequency spectrum, even though the cutoff frequency ranges of the bandpass filters of the breath and heart rate respectively don't intersect. The presence of those harmonics makes selecting the correct peak in the heart waveform's frequency spectrum challenging, as the waveform gets cluttered up with strong peaks corresponding to breath harmonics. This is demonstrated in Fig. 3.39, where the correct peak marked in red is surrounded by harmonics-related noise.

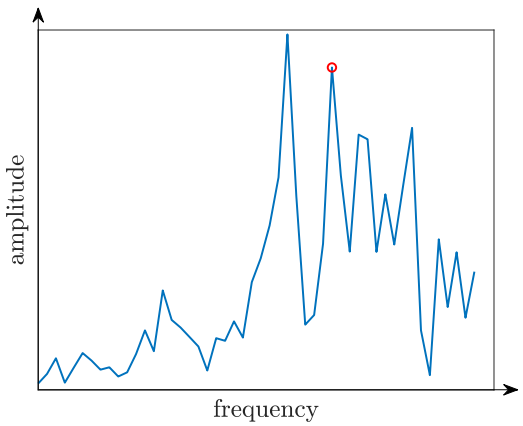

Figure 3.39: Breath harmonics surround the heart rate peak marked in red.

To solve this we use the Kalman-filtered final breath rate estimate, which is most likely to be accurate, and from it we calculate its integral multiples present in the typical heart rate's typical frequency range, which is the same as the heart rate's bandpass filter's cutoff frequencies. Then, using a series notch filters, each with a notch frequency corresponding to a breath harmonic, the breath harmonics get filtered out from the heart waveform. This results in a less cluttered heart waveform frequency spectrum, which enables more accurate heart rate estimation.

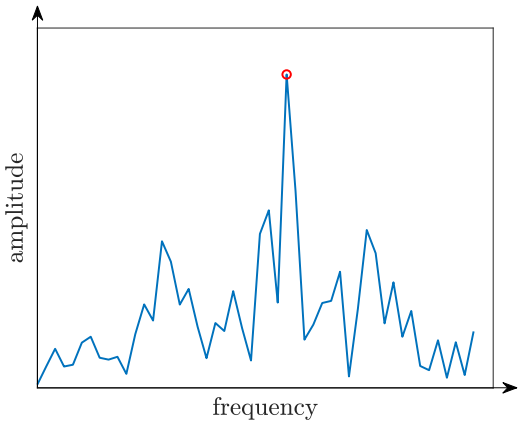

Figure 3.40: A less cluttered heart waveform frequency spectrum.

4 Results

In this chapter, experiments and corresponding results of the vital sign signal processing chain introduced in the previous chapter are presented. The experiments are designed to test the accuracy of the signal processing chain's estimate of the breath and heart rate across a range of different conditions: *physical orientation*, where a subject is either sitting down or standing up; *physical condition*, where the subject's vital signs are measured while they are relaxed, having just exerted effort, or intentionally breathing slowly; *number of subjects*, where the vital signs of up to two subjects are measured simultaneously.

4.1 Radar Hardware

The radar hardware used for experiments was the RADARBOOK by NOFFZ Technologies. This radar could be connected to a computer via an Ethernet cable, and could be interfaced using a provided MATLAB® library.

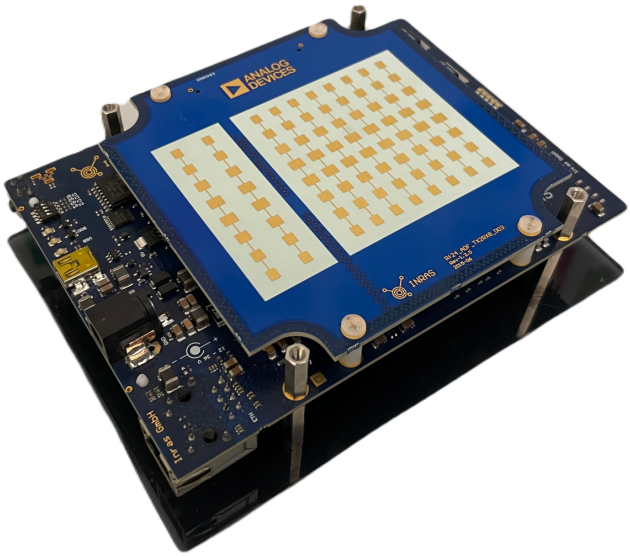

Figure 4.1: The RADARBOOK radar by NOFFZ Technologies.

As seen in Fig. 4.1, the radar has two TX antennas and eight RX antennas. The use of more than one TX antenna enables time-division multiplexing (TDM) which enables high chirp rates. For this application, one TX antenna was sufficient. The radar was configured for a chirp rate of 20 Hz, a value sufficiently higher than the highest frequency possibly expected to be sampled, to satisfy the Nyquist criteria, and prevent any aliasing of the noise. A summary of the radar's configuration is shown in Tab. 4.1.

Parameter	Value
TX Count	1
RX Count	8
Chirp Rate	20 Hz
Operating Frequency	24 GHz
Starting Frequency (f_c)	23.7 GHz
Bandwidth (B)	600 MHz
Chirp Duration (T_c)	1024 μs

Table 4.1: The radar configuration for the experiment.

4.2 Experiment Setup

Six subjects volunteered to participate in the experiments for this work. Each subject was assigned a numeric ID, for anonymity, and convenience of data processing. The relevant properties; gender, age, height, and weight of the participants are shown in Tab. 4.2. The experiments for testing vital sign measurement for one person saw each subject position themselves in front of the radar for each of the six combinations of physical orientation (sitting or standing) and physical condition (relaxed, effort, or slow), for a total of 65 seconds for each combination. So, the total number of single-person experiments conducted is 36.

ID	Gender	Age	Height (cm)	Weight (kg)
1	Male	25	173	81
2	Male	25	172	105
3	Male	28	167	80
4	Male	25	180	89
5	Female	28	162	69
6	Female	25	170	105

Table 4.2: The relevant properties of the participating subjects.

During each experiment, the ground truth values of the subject's vital signs were measured and recorded, from which the vital sign signal processing chain's accuracy could be measured. The raw radar data collected during those 65 seconds along with the vital signs' ground truth values were recorded as `*.mat` files. This would enable accuracy evaluation at a later separate change for convenience purposes, and allows for signal processing chain modifications for tuning purposes.

For each experiment, the breath rate ground truth was measured by asking the subject to count the number of breaths they take between hearing two beeps generated by the data collection computer program which signify the start and end of the 65 seconds respectively, then having the subject report their breath count at the end of the experiment, from which an average value for the whole 65 second window could be calculated. The heart rate ground truth was measured using a the Rad-G™ Pulse Oximeter by Masimo, from which the heart rate at the start and end of the 65 second widow were recorded and their average was used as an average value for the whole 65 second window.

Each experiment saw that for the relaxed physical condition, the subject would be asked to breath normally, and for the slow-breathing physical condition the subject would be asked to breath significantly slower than they normally would. For the effort-exerted physical condition, the subject would be asked to rather quickly climb 50 stair steps in order to induce high breath and heart rates. Each subject's experiment combinations of standing-effort and sitting-effort were the last two combinations to prevent the elevated breath and heart rates from affecting the other combinations. An example experiment is shown in Fig. 4.2.

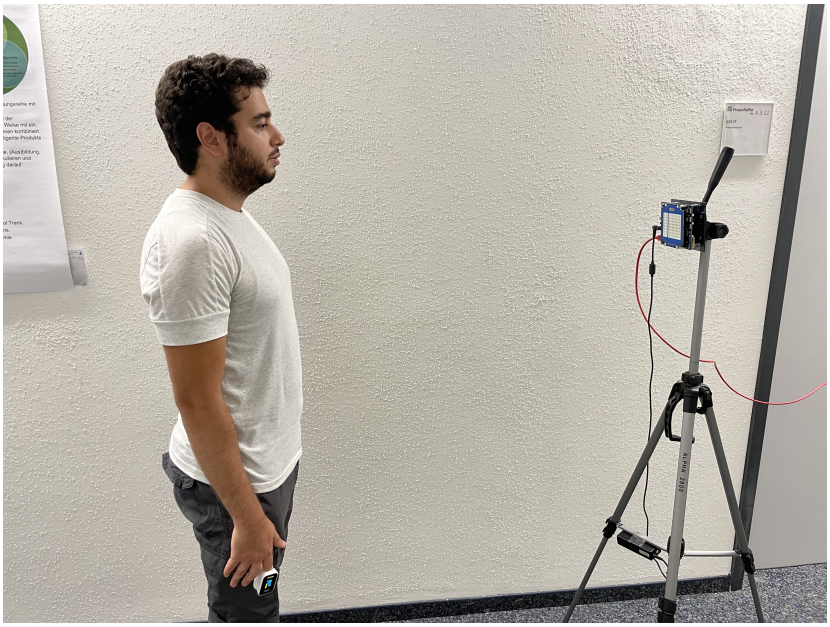

Figure 4.2: An experiment with a relaxed standing subject.

In addition to the single-person experiments, five special-configuration experiments were conducted to test the vital sign signal processing chain's capability of measuring the vital signs of two subjects simultaneously, as well as being able to ignore dead objects positioned next to a live subject. The dead object consisted of a chair seating a sheet of metal, guaranteeing its visibility with respect to the radar. The five additional experiments were configured as

- Two people sitting.
- Two people standing.
- One person sitting one person standing.
- One person sitting next to a dead object.
- One person standing next to a dead object.

4.3 Experiment Results

The individual results of the single-person experiments are shown in Tab. 4.6 and Tab. 4.7 for the breath and heart rates respectively. The error is calculated as the average absolute error over the last 30 seconds of the experiment. This ensured that the Kalman filter estimates had already stabilized. Averaged over the all configurations the error was 0.4 ± 0.3 BPM for the breath rate and 1.4 ± 0.9 BPM for the heart rate. The averaged errors over specific physical orientation and condition combinations are shown in Tab. 4.3 and Tab. 4.4. The average errors on varying only physical orientation are shown in Fig. 4.3, and similarly for physical condition the average errors are shown in Fig. 4.4, for both the breath and heart rates.

	Slow	Relaxed	Effort
Sitting	0.3 ±0.1	0.3 ±0.2	0.4 ±0.1
Standing	0.4 ±0.3	0.5 ±0.2	0.5 ±0.4

Table 4.3: Breath rate errors for different configurations in BPM.

	Slow	Relaxed	Effort
Sitting	1.1 ±0.6	1.3 ±1.0	1.7 ±0.9
Standing	1.0 ±0.2	1.3 ±1.1	2.2 ±1.1

Table 4.4: Heart rate errors for different configurations in BPM.

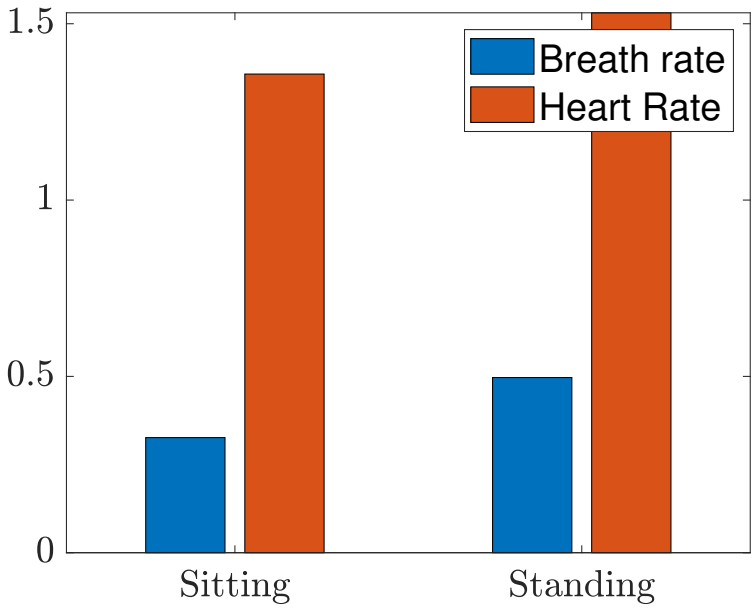

Figure 4.3: Average errors across physical orientations.

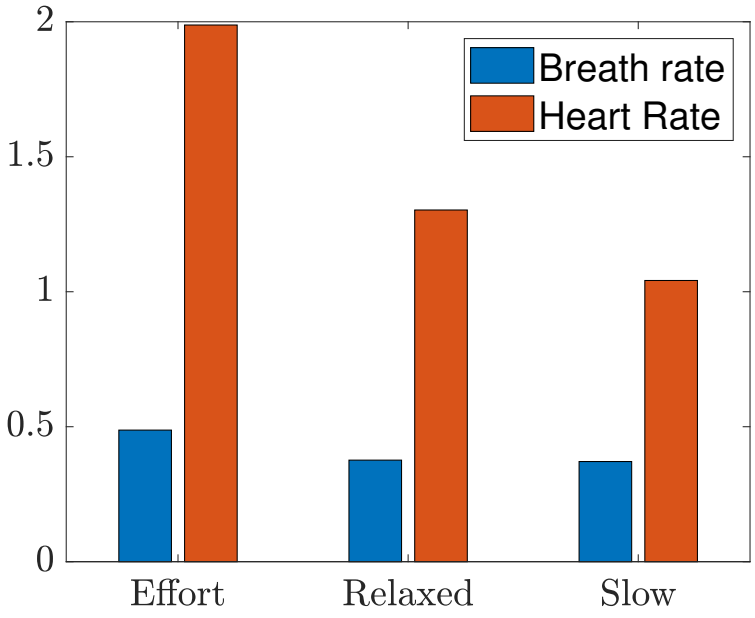

Figure 4.4: Average errors across physical conditions.

The results of the special-configuration experiments are shown in Tab. 4.5 with horizontal lines separating the results of each special-configuration experiment. The first three experiments listed in the Table are double-person experiments, and the other two are single-person experiments with positioning next to a dead object.

Experiment Type	ID	Orientation	State	BR Error (BPM)	HR Error (BPM)
Double-person	5	Sitting	Relaxed	1.3	0.4
	2	Sitting	Relaxed	0.3	0.5
Double-person	5	Standing	Relaxed	0.7	1.2
	2	Standing	Relaxed	0.6	2.7
Double-person	2	Sitting	Relaxed	0.4	0.2
	5	Standing	Relaxed	0.3	1.3
Single-person with dead object	2	Sitting	Relaxed	0.1	2.1
Single-person with dead object	2	Standing	Relaxed	0.3	0.8

Table 4.5: Results of the special-configuration experiments.

ID	Orientation	State	Vital Sign	Error (BPM)
1	Sitting	Effort	BR	0.3
1	Sitting	Relaxed	BR	0.4
1	Sitting	Slow	BR	0.1
1	Standing	Effort	BR	0.4
1	Standing	Relaxed	BR	0.2
1	Standing	Slow	BR	0.3
2	Sitting	Effort	BR	0.4
2	Sitting	Relaxed	BR	0.1
2	Sitting	Slow	BR	0.3
2	Standing	Effort	BR	1.2
2	Standing	Relaxed	BR	0.6
2	Standing	Slow	BR	0.3
3	Sitting	Effort	BR	0.4
3	Sitting	Relaxed	BR	0.1
3	Sitting	Slow	BR	0.4
3	Standing	Effort	BR	0.4
3	Standing	Relaxed	BR	0.7
3	Standing	Slow	BR	0.2
4	Sitting	Effort	BR	0.6
4	Sitting	Relaxed	BR	0.5
4	Sitting	Slow	BR	0.3
4	Standing	Effort	BR	0.3
4	Standing	Relaxed	BR	0.6
4	Standing	Slow	BR	0.9
5	Sitting	Effort	BR	0.5
5	Sitting	Relaxed	BR	0.4
5	Sitting	Slow	BR	0.3
5	Standing	Effort	BR	0.1
5	Standing	Relaxed	BR	0.2
5	Standing	Slow	BR	0.3
6	Sitting	Effort	BR	0.4
6	Sitting	Relaxed	BR	0.2
6	Sitting	Slow	BR	0.4
6	Standing	Effort	BR	0.9
6	Standing	Relaxed	BR	0.7
6	Standing	Slow	BR	0.7

Table 4.6: Breath rate errors per trial.

ID	Orientation	State	Vital Sign	Error (BPM)
1	Sitting	Effort	HR	2.6
1	Sitting	Relaxed	HR	0.4
1	Sitting	Slow	HR	1.7
1	Standing	Effort	HR	1.9
1	Standing	Relaxed	HR	3.5
1	Standing	Slow	HR	0.9
2	Sitting	Effort	HR	0.8
2	Sitting	Relaxed	HR	2.1
2	Sitting	Slow	HR	0.2
2	Standing	Effort	HR	1.8
2	Standing	Relaxed	HR	0.4
2	Standing	Slow	HR	1.2
3	Sitting	Effort	HR	3
3	Sitting	Relaxed	HR	3
3	Sitting	Slow	HR	1.4
3	Standing	Effort	HR	2.5
3	Standing	Relaxed	HR	1.2
3	Standing	Slow	HR	0.8
4	Sitting	Effort	HR	1.8
4	Sitting	Relaxed	HR	0.4
4	Sitting	Slow	HR	1.5
4	Standing	Effort	HR	1.6
4	Standing	Relaxed	HR	0.7
4	Standing	Slow	HR	1.2
5	Sitting	Effort	HR	0.9
5	Sitting	Relaxed	HR	0.8
5	Sitting	Slow	HR	0.5
5	Standing	Effort	HR	4.3
5	Standing	Relaxed	HR	0.9
5	Standing	Slow	HR	0.9
6	Sitting	Effort	HR	1.3
6	Sitting	Relaxed	HR	0.9
6	Sitting	Slow	HR	1
6	Standing	Effort	HR	1.3
6	Standing	Relaxed	HR	1.3
6	Standing	Slow	HR	1.1

Table 4.7: Heart rate errors per trial.

4.4 Experiment Results Discussion

Using the averaged errors over all configurations of 0.4 ± 0.3 BPM for the breathing rate and 1.4 ± 0.9 BPM for the heart rate, and comparing to typical ranges of [12, 16] BPM for the breath rate and [60, 100] BPM for the heart rate of resting adults, it can be seen that the error values are acceptable. It can be seen from Fig. 4.3 that standing instead of sitting down will slightly increase the error for both the breath and the heart rates. This error increase is expected, since standing has the effect of adding random-body-motion-related effects to the phase signal, making it more noisy. Nevertheless, this increase in error is slight and acceptable. On the other hand, Fig. 4.4 shows that going from a slow-breathing physical condition to an effort-exerted physical condition will only slightly increase the breath rate error, but it will almost double the heart rate error, meaning that being in a more effort-exerted state has a more profound effect on the heart rate. This could most likely be explained by the fact that being in a more effort-exerted state corresponds to stronger breathing causing the chest wall motion due to breathing to dwarf that of the heart beat, which is already comparatively small. Still, such errors are within the acceptable range.

4.5 GUI

To interface with the radar and display live vital sign readings of up to two subjects, an interactive GUI application has been developed. In Fig. 4.5 the application is shown for the running example of Chap. 3, where two subjects are present, with one subject sitting down and the other standing up, and a chair between them.

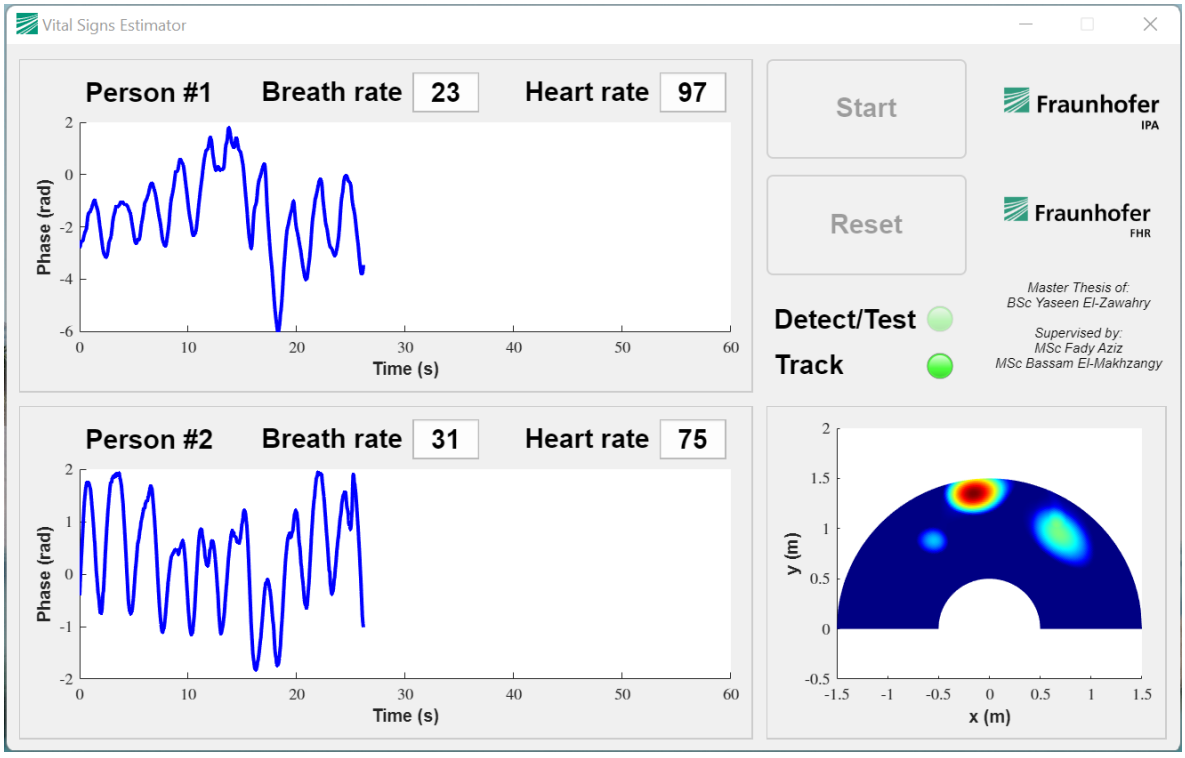

Figure 4.5: The GUI application interfaces with the radar and displays results.

The GUI application displays the breath and heart rates of each subject in the respective field. By the convention shown in Fig. 3.3, subjects #1 and #2 are the ones on the right and left, respectively, looking forward from the radar. The phase variations of both subjects are also visualized, confirming the liveliness of the detected objects. In case only one person is present, then only the first field will visualize results, and in case no subjects are detected, then none of the fields will visualize results.

5 Conclusion

Using radars to measure human vital signs in a contactless fashion is a more convenient, comfortable, and long-term practical method as compared to classical contact-based technology. Achieving standard medical accuracy of vital sign measurement requires the development of signal processing algorithms that are accurate, and robust in the face of change of physical orientation and condition. Adding the capability to measure the vital signs of more than one person is also desirable, as it improves the utilization of a single piece of radar hardware at the same cost. This thesis set to tackle the aforementioned points from increasing robustness to adding the capability to measure the vital signs of more than one person. For this, we chose an FMCW radar, which possesses an ability to detect multiple targets' ranges and angles, as well as a sensitivity to millimeter level changes in range, which is required to pick up the minute chest-wall motion due to breathing and the heart beat.

5.1 Summary

We started in Chap. 2 by introducing the needed FMCW radar theory of operation, the structure of the raw data; and how it could be used to estimate range and the angle of incidence; and how it could be used to create a range-angle heat map. In Chap. 3 we showed step by step how a series of raw radar data could be used to finally come up with an estimate of the breath and heart rate for multiple subjects simultaneously. Then In Chap. 4 we introduced the experiment setup including the chosen piece of radar hardware, the corresponding experiment results, and the GUI application developed to interface with the radar and produce real-time vital sign estimates for up to two subjects simultaneously. The results indicated satisfactory performance of the radar and the vital signs signal processing chain to produce breath and heart rate estimates for across multiple physical orientations and conditions, as well as a clear capability to estimate vital signs for up to two subjects and also differentiate between live and dead objects.

5.2 Limitations and Future Work

This thesis took estimation of vital signs using radars a step forward, adding new capabilities and improving reliability of contactless vital sign measurement. However, this is not where research in this topic ends. Limitations to this work include

- Limiting subjects to one physical orientation and now allowing them to move.
- Limiting the position of the radar to a fixed position during measurement.
- Using averaging to create ground truth values and discarding intermediate variations.
- Classical signal processing techniques are not the most advanced methods available.

Such limitations along with the presented work could be used as a starting point for future work that could improve the reliability and robustness of contactless vital sign measurement even further. Suggestions correspondingly include

- Researching how to allow subjects to move and change position during measurement.
- Researching how to fix the radar to a platform that moves during measurement (e.g. a drone).
- Using vital sign measuring equipment that can interface with the data collection computer program to maintain intermediate variations in the vital sign ground truth values.
- Investigating the use of deep learning methods to estimate vital signs.

List of Figures

List of Tables

Bibliography

[1] M. Kebe, R. Gadhafi, B. Mohammad, M. Sanduleanu, H. Saleh and M. Al-Qutayri, "Human vital signs detection methods and potential using radars: A review," *Sensors*, vol. 20, no. 5, p. 1454, Mar. 2020. [Online]. Available: https://doi.org/10.3390/s20051454

[2] K. Valentine, N. Ayas, P. Eastwood, R. Heinzer, M. Ip, S. Patel, P. Peppard, S. Sinha, S. Tufik, C. Nunez and A. Malhotra, *Global Prevalence of Obstructive Sleep Apnea in Adults: Estimation Using Currently Available Data*, pp. A3962–A3962. [Online]. Available: https://www.atsjournals.org/doi/abs/10.1164/ajrccm-conference.2018.197.1_MeetingAbstracts.A3962

[3] Sudden unexpected infant death and sudden infant death syndrome. [Online]. Available: https://www.cdc.gov/sids/index.htm

[4] E. Helfenbein, R. Firoozabadi, S. Chien, E. Carlson and S. Babaeizadeh, "Development of three methods for extracting respiration from the surface ECG: A review," *Journal of Electrocardiology*, vol. 47, no. 6, pp. 819–825, Nov. 2014. [Online]. Available: https://doi.org/10.1016/j.jelectrocard.2014.07.020

[5] T. Rantonen, J. Jalonen, J. Grönlund, K. Antila, D. Southall and I. Välimäki, "Increased amplitude modulation of continuous respiration precedes sudden infant death syndrome," *Early Human Development*, vol. 53, no. 1, pp. 53–63, Nov. 1998. [Online]. Available: https://doi.org/10.1016/s0378-3782(98)00039-5

[6] Cardiovascular diseases. [Online]. Available: https://www.who.int/health-topics/cardiovascular-diseases/#tab=tab_1

[7] J. L. ATLEF, "Principles of clinical electrocardiography," *Anesthesiology*, vol. 52, no. 2, pp. 195–195, Feb. 1980. [Online]. Available: https://doi.org/10.1097/00000542-198002000-00038

[8] D. N. Dutta, R. Das and S. Pal, "Automated real-time processing of single lead electrocardiogram for simultaneous heart rate and respiratory rate monitoring," *Journal of Medical Devices*, vol. 11, no. 2, May 2017. [Online]. Available: https://doi.org/10.1115/1.4035982

[9] L. Stingeni, E. Cerulli, A. Spalletti, A. Mazzoli, L. Rigano, L. Bianchi and K. Hansel, "The role of acrylic acid impurity as a sensitizing component in electrocardiogram electrodes," *Contact Dermatitis*, vol. 73, no. 1, pp. 44–48, Jan. 2015. [Online]. Available: https://doi.org/10.1111/cod.12357

[10] J. Allen, "Photoplethysmography and its application in clinical physiological measurement," *Physiological Measurement*, vol. 28, no. 3, pp. R1–R39, Feb. 2007. [Online]. Available: https://doi.org/10.1088/0967-3334/28/3/r01

[11] T. Tamura, Y. Maeda, M. Sekine and M. Yoshida, "Wearable photoplethysmographic sensors—past and present," *Electronics*, vol. 3, no. 2, pp. 282–302, Apr. 2014. [Online]. Available: https://doi.org/10.3390/electronics3020282

[12] M. Ghamari, "A review on wearable photoplethysmography sensors and their potential future applications in health care," *International Journal of Biosensors &amp Bioelectronics*, vol. 4, no. 4, 2018. [Online]. Available: https://doi.org/10.15406/ijbsbe.2018.04.00125

[13] G. G. BERNTSON, J. T. CACIOPPO and K. S. QUIGLEY, "Respiratory sinus arrhythmia: Autonomic origins, physiological mechanisms, and psychophysiological implications," *Psychophysiology*, vol. 30, no. 2, pp. 183–196, Mar. 1993. [Online]. Available: https://doi.org/10.1111/j.1469-8986.1993.tb01731.x

[14] C. Massaroni, A. Nicolò, D. L. Presti, M. Sacchetti, S. Silvestri and E. Schena, "Contact-based methods for measuring respiratory rate," *Sensors*, vol. 19, no. 4, p. 908, Feb. 2019. [Online]. Available: https://doi.org/10.3390/s19040908

[15] J. M. Moll and V. Wright, "An objective clinical study of chest expansion." *Annals of the Rheumatic Diseases*, vol. 31, no. 1, pp. 1–8, Jan. 1972. [Online]. Available: https://doi.org/10.1136/ard.31.1.1

[16] H. Lin, W. Xu, N. Guan, D. Ji, Y. Wei and W. Yi, "Noninvasive and continuous blood pressure monitoring using wearable body sensor networks," *IEEE Intelligent Systems*, vol. 30, no. 6, pp. 38–48, Nov. 2015. [Online]. Available: https://doi.org/10.1109/mis.2015.72

[17] K. Uemura, T. Kawada and M. Sugimachi, "A novel minimally occlusive cuff method utilizing ultrasound vascular imaging for stress-free blood pressure measurement: A-proof-of-concept study," *IEEE Transactions on Biomedical Engineering*, vol. 66, no. 4, pp. 934–945, Apr. 2019. [Online]. Available: https://doi.org/10.1109/tbme.2018.2865556

[18] K. Shioya and T. Dohi, "Blood pressure measurement device based on the arterial tonometry method with micro triaxial force sensor," in *2013 Transducers &amp Eurosensors XXVII: The 17th International Conference on Solid-State Sensors, Actuators and Microsystems (TRANSDUCERS &amp EUROSENSORS XXVII)*. IEEE, Jun. 2013. [Online]. Available: https://doi.org/10.1109/transducers.2013.6627287

[19] A. K. Abbas and R. Bassam, "Phonocardiography signal processing," *Synthesis Lectures on Biomedical Engineering*, vol. 4, no. 1, pp. 1–194, Jan. 2009. [Online]. Available: https://doi.org/10.2200/s00187ed1v01y200904bme031

[20] S. Ismail, I. Siddiqi and U. Akram, "Localization and classification of heart beats in phonocardiography signals —a comprehensive review," *EURASIP Journal on Advances in Signal Processing*, vol. 2018, no. 1, Apr. 2018. [Online]. Available: https://doi.org/10.1186/s13634-018-0545-9

[21] R. Zalter, H. Hodara and A. A. Luisada, "Phonocardiography," *The American Journal of Cardiology*, vol. 4, no. 1, pp. 3–15, Jul. 1959. [Online]. Available: https://doi.org/10.1016/0002-9149(59)90188-2

[22] R. Ichapurapu, S. Jain, M. U. Kakade, D. Y. Lie and R. E. Banister, "A 2.4ghz non-contact biosensor system for continuous vital-signs monitoring on a single PCB,"

in *2009 IEEE 8th International Conference on ASIC*. IEEE, Oct. 2009. [Online]. Available: https://doi.org/10.1109/asicon.2009.5351542

[23] Y. S. Lee, P. N. Pathirana, T. Caelli and S. Li, "Further applications of doppler radar for non-contact respiratory assessment," in *2013 35th Annual International Conference of the IEEE Engineering in Medicine and Biology Society (EMBC)*. IEEE, Jul. 2013. [Online]. Available: https://doi.org/10.1109/embc.2013.6610380

[24] A. Høst-Madsen, N. Petrochilos, O. Boric-Lubecke, V. M. Lubecke, B.-K. Park and Q. Zhou, "Signal processing methods for doppler radar heart rate monitoring," in *Signal Processing Techniques for Knowledge Extraction and Information Fusion*. Springer US, 2008, pp. 121–140. [Online]. Available: https://doi.org/10.1007/978-0-387-74367-7_7

[25] Y. Xu, S. Dai, S. Wu, J. Chen and G. Fang, "Vital sign detection method based on multiple higher order cumulant for ultrawideband radar," *IEEE Transactions on Geoscience and Remote Sensing*, vol. 50, no. 4, pp. 1254–1265, Apr. 2012. [Online]. Available: https://doi.org/10.1109/tgrs.2011.2164928

[26] S. D. Liang, "Sense-through-wall human detection based on UWB radar sensors," *Signal Processing*, vol. 126, pp. 117–124, Sep. 2016. [Online]. Available: https://doi.org/10.1016/j.sigpro.2015.09.022

[27] Z. Zhang, Y. Nian, J. Chen and M. He, "An experimental study to optimize the stepped-frequency continuous-wave radar parameters for noncontact multi-target vital sign monitoring," in *2019 IEEE International Conference on Computational Electromagnetics (ICCEM)*. IEEE, Mar. 2019. [Online]. Available: https://doi.org/10.1109/compem.2019.8779202

[28] L. Liu and S. Liu, "Remote detection of human vital sign with stepped-frequency continuous wave radar," *IEEE Journal of Selected Topics in Applied Earth Observations and Remote Sensing*, vol. 7, no. 3, pp. 775–782, Mar. 2014. [Online]. Available: https://doi.org/10.1109/jstars.2014.2306995

[29] H. Lee, B.-H. Kim, J.-K. Park and J.-G. Yook, "A novel vital-sign sensing algorithm for multiple subjects based on 24-GHz FMCW doppler radar," *Remote Sensing*, vol. 11, no. 10, p. 1237, May 2019. [Online]. Available: https://doi.org/10.3390/rs11101237

[30] A. Ahmad, J. C. Roh, D. Wang and A. Dubey, "Vital signs monitoring of multiple people using a FMCW millimeter-wave sensor," in *2018 IEEE Radar Conference (RadarConf18)*. IEEE, Apr. 2018. [Online]. Available: https://doi.org/10.1109/radar.2018.8378778

[31] T. Helal, "Enhanced contactless respiratory rate estimation in standing position using millimeter wave radar," Master's thesis, University of Stuttgart, 2021.

[32] Fourier transform. [Online]. Available: https://en.wikipedia.org/wiki/Fourier_transform

[33] R. E. Kalman, "A new approach to linear filtering and prediction problems," *Journal of Basic Engineering*, vol. 82, no. 1, pp. 35–45, Mar. 1960. [Online]. Available: https://doi.org/10.1115/1.3662552

Declaration

Herewith, I declare that I have developed and written the enclosed thesis entirely by myself and that I have not used sources or means except those declared.

This thesis has not been submitted to any other authority to achieve an academic grading and has not been published elsewhere.

Stuttgart, 31.07.2022 Yaseen El-Zawahry